Profile distortion by beam space-charge in Ionization Profile Monitors

Dominik Vilsmeier

April 21, 2015

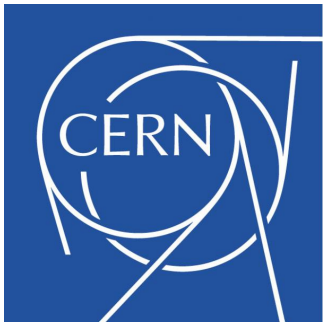

Supervisors:

Prof. Dr. Tilo Wettig **Dr. Mariusz Sapinski**

Abstract

Measuring the transverse beam size in the Large Hadron Collider by using Ionization Profile Monitors is a difficult task for energies above injection during the energy ramp from 450 GeV to 6.5 TeV. The beam size decreases from around $1\,mm$ to $200\,\mu m$ and the brightness of the beam is high enough to destroy the structure of any form of interacting matter. While the electron trajectories are confined by an external electro-magnetic field which forces the electrons accordingly on helix paths with certain gyroradii, this gyration is heavily increased under the influence of the electric field of the beam. Smaller beam sizes, which go hand in hand with increased bunch electric fields, lead to larger gyroradii of the ionized electrons, which results in strongly distorted profiles. In addition, this distortion becomes more visible for smaller beam sizes as the extent of gyration grows compared to the actual beam size.

Depending on the initial momentum distribution of the electrons, emerging from the ionization process with the highly relativistic beam, the profile distortion is affected significantly. In order to be able to perform reliable investigations into the effects of space charge a good knowledge of such initial momentum distributions is essential. The theoretical calculation of electron initial momenta will be discussed in order to obtain reliable results from the simulation of the electron movement within the ionization chamber which are used to investigate the effect of space charge on the registered profiles.

An analytical approach to the mechanism of profile distortion is presented, which is based on the increased gyration of electrons after they left the space charge region. Their parallel movement close to the detector is unaffected by the bunch field and can therefore be described as a purely circular movement. A description of the profile distortion for single gyroradii, which is based on convolution, is built upon that mechanism along with the option of restoring the corresponding initial profile.

A method for the correction of the registered profiles is presented, which is based on the partitioning of the detector profile with respect to the gyroradii of electrons. The distortion of the emerging partial profiles is described via convolution with corresponding point spread functions. Partial corrections can be obtained via deconvolution and together they yield the beam profile. A way of separating the electron signal with respect to the gyroradius in the form of an electron sieve is presented as well.

Contents

List of Figures

1. Introduction

Founded in 1954 CERN has evolved into the biggest research institute in the world. Its main goal is to study the structure of the universe and the bits it consists of. For this purpose various particle accelerators have been built over the years leading to the largest and most powerful accelerator in the world, the Large Hadron Collider (LHC). With a circumference of 27 km and operation of superconducting magnets at temperatures of 1.9 K - reaching magnetic field strengths of more than 8 T - it provided during Run 1 in 2012 proton beams of up to 4 TeV for the four main experiments around the ring. For the second run in 2015 a maximum beam energy of 6.5 TeV is scheduled.

Before injected in the LHC - at an energy of 450 GeV - the protons run through multiple stages of prior acceleration performed by several other accelerators. To observe and accordingly control the operation of particle accelerators it is important to have advanced and reliable beam instruments. Parameters that must be measured are for example the position of the beam (and therefore its offset from the design orbit), its intensity, the bunch length, beam losses (in order to prevent quenching of the superconducting magnets and to protect the equipment in general) and the transverse beam size.

Amongst other devices Ionization Profile Monitors (IPM) are used in the LHC to measure the transverse beam size. Because of the high brightness of the LHC beam devices that are based on direct interaction with the beam (like Wire Scanners) cannot be used. The brightness of the beam is high enough to destroy any interacting part of a beam instrument in a short time period. The advantage of Ionization Profile Monitors is the technique of indirect profile measurement via gas ionization.

In order to keep the particles on the design orbit a circular collider, such as the LHC, uses several components. Dipole magnets are used to bend the beam on the circular path of the beam pipe. Because the particles have a momentum transverse to the design orbit they start deviating from it and quadrupole magnets are used to focus them back. Because the magnetic fields of a quadrupole magnet are proportional to the offset from the center with respect to the perpendicular direction ($B_x \propto y$, $B_y \propto x$), a quadrupole magnet focuses the beam in one transverse direction and defocuses it simultaneously in the other direction. That is why quadrupole magnets with alternated polarisation are used along the beam line. Thus the particles oscillate around the design orbit in the transverse plane while they are moving in the beam pipe. Due to those oscillations the transverse beam size depends on the setup of the accelerator (that is on the distance to the quadrupole magnets and their focal strength) as well as on the transverse momentum spread of particles and the beam size at injection. For each point around the ring the particles occupy a volume in the trace space xx' and while the shape of this volume changes along the ring (according to the optical functions of the quadrupole magnets) its magnitude remains constant. The area covered by the phase space ellipse is defined as the *transverse emittance* and depends on initial conditions. However for a real beam other effects such as intra-beam scattering and beam-beam effects can change the transverse movement of particles and thus cause a change of transverse emittance. The purpose of Ionization Profile Monitors is to measure the transverse beam size in order to observe the behaviour of transverse emittance during the machine cycle.

2. Ionization Profile Monitors

The idea behind Ionization Profile Monitors is to measure the transverse beam profile indirectly via an equivalent electron distribution which is generated in ionization by interaction of the beam with gas atoms. For this purpose a low pressure gas is artificially injected into the vacuum chamber in order to provide a sufficient number of electrons from ionization. For a homogeneous gas density in the ionization chamber the emerging electron distribution will represent the transverse shape of the beam profile. The effect of gas burnout (a decrease in relevant gas density due to ionization) has been estimated not to play a role because the gas diffusion towards the crucial volume compensates any decrease in density fast enough, that is the distribution of the gas can be considered to be homogeneous during the whole operation. An external electric field is used to guide the ions towards the cathode where they recombine as well as the electrons towards the anode. Some IPMs are designed to detect ions while the ones installed in the LHC detect electrons. The detector system consists of a multi-channel plate (MCP) for amplifying the electron signal, a phosphor screen which converts the electron signal into light and an optical system with a camera in the end which finally measures the amount of light which is proportional to the transverse beam profile that is parallel to the MCP (see Fig. 1).

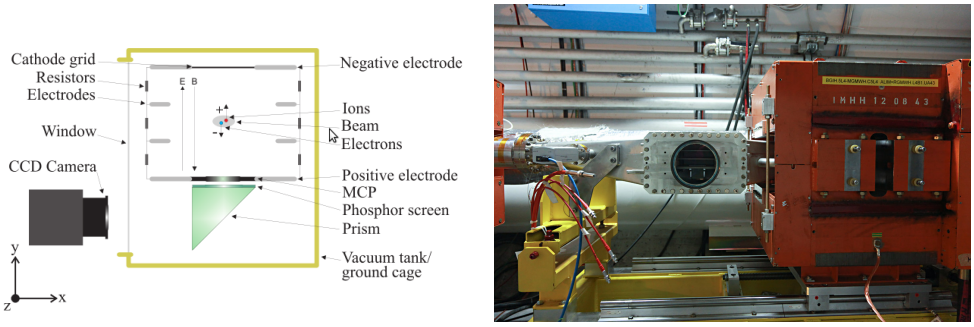

Figure 1: Left: Operating principle of an Ionization Profile Monitor [2, H.Refsum]. Right: Picture of one of the horizontal devices in the LHC; the magnet (orange) is shifted, the window for the camera is visible [2].

In the ideal case all electrons are guided on straight lines towards the detector system implying that no displacement of electrons with respect to their ionization positions occurs. However because the electrons obtain an initial momentum from the ionization process which causes a movement that is parallel to the detector system, their paths will describe parabolic trajectories instead of straight lines. This causes a displacement from their original positions in the parallel plane at the detector leading to a recorded profile which is different from the initial beam profile. In order to suppress this effect an additional magnetic field, aligned together with the electric extraction field, is installed. This magnetic field forces the electrons to perform a circular movement in the plane parallel to the detector, constraining their maximal displacement. The resulting movements are helix trajectories whose radii are determined by the initial velocities of electrons and the strength of the magnetic field.

In addition the electrons in the ionization chamber interact with the electric field of the beam (known as *space charge effects*) whereupon for high beam energies this field gets so

strong that the helix trajectories of electrons are affected significantly in form of an increase of gyration and the magnetic field is no more sufficient to suppress possible displacements. Those possible displacements of electrons lead to a noticeable profile distortion at the detector. The resulting gyroradii, depending on the initial conditions of electrons as well as on the beam parameters, determine the distortion of the profile.

Several investigations on beam space-charge induced profile distortion have already been performed in [5, 10]. The subject of this work is - amongst others - to investigate the basic causes of the profile distortion in order to build a reliable method of profile correction upon it.

The following coordinate system will be used throughout the paper (compare Fig. 1):

z – direction in which the beam is moving

x – direction along which we want to measure the transverse (with respect to z) beam profile

y – transverse to x and z, direction towards the detector

The investigations presented in this work - in form of simulation studies - are performed for the configuration of the vertical device of beam 2 in the LHC. The corresponding optical functions are $\beta_x = 213\,\mathrm{m}$ and $\beta_y = 271\,\mathrm{m}$ (for Run 1). Table 1 shows the beam parameters for typical configurations of the LHC beam where the first two are actual configurations from Run 1 in 2012 and the third one is a scheduled configuration for Run 2 in 2015.

parameter	**450 GeV**	**4 TeV**	**6.5 TeV**
emittance [μm]	1.7	2.4	1.7
bunch			
- intensity [10^{11} ppb]	1.5	1.7	1.3
- length ($4\sigma_z$) [ns]	1.2	1.2	1.25
σ_{beam} [μm]	869	346	229

Table 1: Simulated cases that have been studied in detail.

3. Simulation of the electron movement in the IPM chamber

In order to study the profile distortion and the effect of beam parameters on it a simulation of the electron movement in the IPM chamber has been established. This simulation is an adapted and simplified version of the PyECLOUD [7] code which was written at CERN in order to study electron cloud built-ups in particle accelerators. The external electric and magnetic fields which are not part of the original version have been added. The fields are assumed to be perfectly aligned, pointing uniformly in opposite y-direction.

The simulation assumes a two-dimensional, transversely sliced beam whose electric field is fully transversal and only acts within this plane. This assumption is valid for highly relativistic beams where the squeezing of the electric field in transverse direction allows to neglect the longitudinal component. The bunch electric field is precalculated on a two-dimensional grid which forms the basis for linear interpolation of its values during the simulation. For the precalculation of the bunch field the formulation of the electric field of an elliptical Gaussian bunch, made by Basetti and Erskine [1], is used. During the simulation the bunch will be advanced, providing subsequent slices for the simulation. Its electric field is scaled according to the current longitudinal charge density. The drift of electrons along the bunch (in z-direction) is neglected because its extent is minor compared to the amount that the bunch moves in the same time. The simulation starts with a bunch offset of $4\sigma_z$ with respect to its longitudinal position.

Mirror charges on the metallic IPM chamber are not taken into account because the size of the chamber is big compared to the region in which the electrons move during the presence of the bunch. Average extraction times without the presence of a bunch are around 3.2 ns, a typical bunch length is around 1.2 ns and the bunch spacing is at least 25 ns. The magnetic field of the beam is neglected as its effect is small compared to the other fields because electron velocities are small when they move close to the bunch ($v \ll c$). Electron-electron interaction is also neglected because of its minor effect compared to the other acting fields.

The simulation is divided into time steps, the positions and velocities of the electrons are updated accordingly and the bunch is advanced in the two-dimensional window. In addition new electrons are generated each time step with positions according to the transverse beam profile. The generation of initial velocities of electrons is not covered directly by the simulation code but has to be provided in form of a separate model (for example data sheets or cross sections). The initial values of newly generated electrons are stored. In addition electrons are checked each time step whether they reached the detector level and the final values of those that did are stored as well. The detector system - consisting of a multi-channel plate, a phosphor screen and an optical system (see Fig. 1) - is not included in the simulation. Initial and final values of electrons are stored in such a way that they can be mapped to each other afterwards.

4. Initial velocities of electrons from ionization

When speaking of initial velocities in the following we mean those velocities that the electrons obtain from the ionization process. The initial velocities - going hand in hand with a gyration parallel to the detector - already imply a potential displacement of electrons which then is enlarged by space charge interaction (for details on the distortion see section 5). Because the electric field of the bunch is weak at the tails of the bunch distribution (compare Fig. 8) almost no enlargement of gyroradii occurs for electrons produced at these positions. If the initial velocities are small then the distortion at the tails is minor, basically not changing the distribution there. However in case of large initial velocities they are sufficient to cause a noticeable distortion, also at the tails of the distribution, leading to a completely different shape of the detected profile.

4.1. Generation of velocities with Geant4

Previously the initial velocity distribution has been generated by the use of Geant4 [6] for the simulation of the ionization process. This distribution turned out to be heavily overestimated in terms of kinetic energy as the concept based on the Bethe formula for energy loss of charged particles in a medium is limited towards small losses depending on the properties of the medium. The kinetic energy of the incident particle must be high enough in order to not collect any ionized electrons and accordingly reduce its charge.

No electrons below a certain threshold ($E_{kin} \approx 100\,\mathrm{eV}$) are generated by Geant4. The most frequent value of the resulting gyroradius distribution is around $300\,\mu m$ which is large compared to a beam size of $346\,\mu m$ (for 4 TeV, see table 1). Therefore a significant enlargement of the tails could be observed as well as a completely different shape of the resulting profile as shown in Fig. 2.

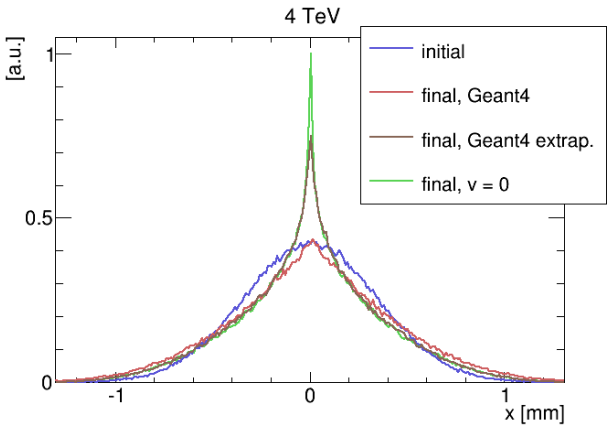

Figure 2: Comparison of the effect of different initial velocity distributions on the registered profiles (denoted by *final*). *Initial* denotes the original beam profile. The obtained results include space charge effects.

Because Geant4 cannot generate electrons with kinetic energies below this certain threshold the idea was to extrapolate the valid data from above this threshold while preserving the

correlations between the momentum components. As expected the correlation between p_x and p_y shows a radial symmetry because none of the two directions is preferred in the ionization process (compare Fig. 3). Extrapolating this radial dependency to zero provides data for p_x and p_y. Although the longitudinal component p_z is small due to the very short interaction time and squeezing of the electric field of the relativistic projectiles in transverse direction the correlation between it and the others should be preserved. Taking the correlation between the transverse component

$$p_t \equiv \sqrt{p_x^2 + p_y^2}$$

and the longitudinal component p_z into account and extrapolating the data accordingly one obtains data for p_x, p_y, p_z while preserving the initial correlations. Figure 4 shows the single differential cross section obtained from the Geant4 data and its extrapolated complement.

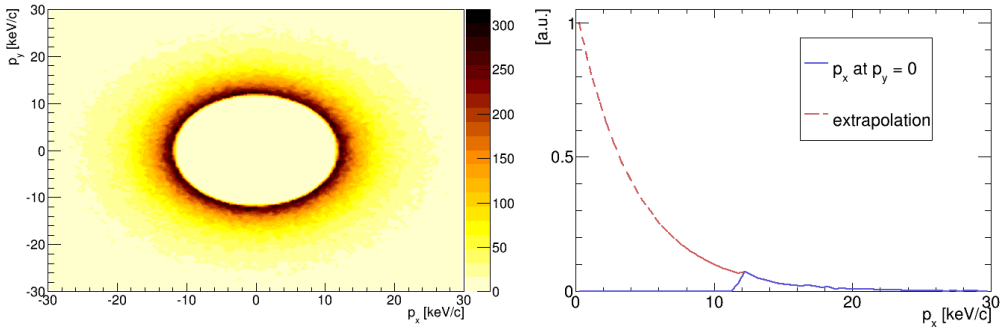

Figure 3: Left: Geant4 data for the correlation between p_x and p_y. Right: Interpolation for p_x at $p_y = 0$ (reflects the radial dependency of the $p_x - p_y$-correlation).

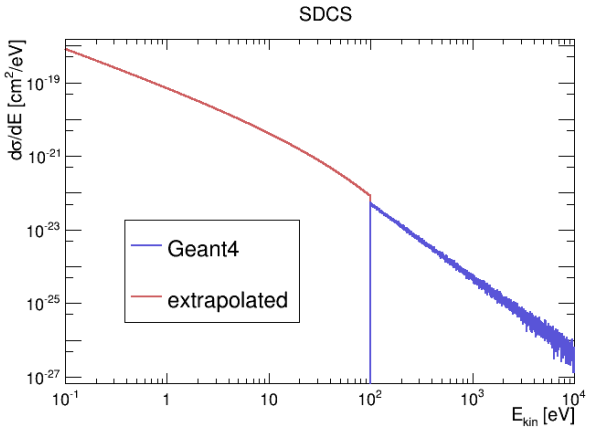

Figure 4: Single differential cross section resulting from the extrapolation of the Geant4 data for electron momenta.

Figure 2 shows a comparison between profiles obtained by using the raw Geant4 data, the extrapolated set and the case for which electrons were produced at rest. As one can see the profile for the extrapolated data almost matches the one for electrons at rest resulting from the strong favouring of low energy electrons in the ionization cross section (compare Fig. 4).

4.2. Ionization cross sections

In order to obtain more precise and reliable values for the initial momenta of electrons their generation by use of a double differential cross section was established. Such a cross section must account for the following aspects:

- highly relativistic protons (up to 7 TeV)
- complex atomic structures (Neon)
- soft emitted electrons (low energies)

The available literature lists many experiments that have been performed for energies in the magnitude of MeV but only a few consider cases for really highly relativistic particles [8, pp. 61-63]. Amongst the various theoretical approaches two were especially promising which are presented in the following.

4.2.1. Bethe approximation

The Bethe approximation for ionization cross sections for charged particles has been established in 1930 by Hans Bethe [3]. It was originally formulated for non-relativistic particles and later extended to a version for relativistic projectiles. It introduces the concept of dipole oscillator strengths in order to account for ionization from the different shells of an atom. The total ionization cross section is obtained as [8, eq.(2.23)]:

$$\sigma_i(T) = \frac{4\pi a_0^2 Z_0^2 R}{T}\left[a_i \ln\left(\frac{T}{R}\right) + b_i + c_i\frac{R}{T} + \dots\right] \tag{1}$$

with the Bohr radius a_0, the Rydberg constant R, the modified kinetic energy $T = m_e v^2/2$ with the projectile velocity v and the projectile charge number Z_0. In consideration of incident protons we set $Z_0 = 1$ in the following. The material dependent coefficients a_i, b_i, c_i depend on the dipole oscillator strengths which can be derived from experimental data for photo-ionization cross sections. Treating the (almost instantaneous) interaction of an atom with a very fast projectile ($v \approx c$) is closely related to the excitation with a fast laser pulse. This correlation helps for calculating the coefficients of the cross section in the Bethe approximation as they can be obtained from experiments using laser excitation which are easier to establish than experiments with particle accelerators. Kim and Rudd give a power series fit for the differential oscillator strengths for various gases [9, table 1].

Non-relativistic formulation

Kim and Rudd derive an expression for the non-relativistic formulation of the single differential ionization cross section in the Bethe approximation [13, eq.(22)]:

$$\frac{d\sigma}{dW} = \frac{4\pi a_0^2 R}{T}\sum_j \left[a_j(E_j)\ln\left(\frac{T}{R}\right) + b_j(E_j) + c_j(E_j)\frac{R}{T} + ...\right] \tag{2}$$

where W is the kinetic energy of the electron, $E_j = W + I_j$ the energy loss of the incident particle, I_j the ionization potential of shell j, $T = m_e v^2/2$ the modified kinetic energy with the projectile velocity v, R the Rydberg constant and a_0 the Bohr radius.

The first coefficient is $a_j(E_j) = (df/dE_j)(R/E_j)$ with the material dependent *dipole oscillator strengths* df/dE_j which are approximated by the following series expansion [9, p.3958]:

$$\frac{df}{d\frac{E_j}{B}} = ay + by^2 + cy^3 + dy^4 + ey^5 + fy^6 + gy^7 \quad , \quad y = \frac{B}{E_j} \tag{3}$$

where E_j is the corresponding photon energy and B is the binding energy (ionization potential) of the atom. The coefficients of this series have been measured for various materials and can be found in [9, table 1]. The independence of the dipole oscillator strengths from the energy of the incident particle holds only in the plane-wave Born approximation [8, p.9].

Relativistic formulation

For a relativistic formulation of the single differential cross section in the Bethe approximation one has to rewrite the term T/R because $v \approx c$ and thus $mv^2/2$ does not represent the kinetic energy of an electron of the same speed. Using $R = m_e c^2 \alpha^2/2$ leads to $T/R = \beta^2/\alpha^2$ with $\beta = v/c$ and the fine structure constant α.

Kim and Rudd also present the single differential cross section in relativistic formulation [13, eq.(22a)]:

$$\frac{d\sigma}{dW} = \frac{4\pi a_0^2 \alpha^2}{\beta^2} \sum_j \left[a_j(E_j) \left[\ln\left(\frac{\beta^2}{1-\beta^2}\right) - \beta^2 \right] + b'_j(E_j) + ... \right] \tag{4}$$

where $b'_j(E_j) = b_j(E_j) - 2a_j(E_j)\ln\alpha$.

The total ionization cross section becomes [8, eq.(2.29),(2.30)]:

$$\sigma_i(\beta^2) = \frac{4\pi a_0^2 \alpha^2}{\beta^2} \left[a_i \ln\left(\frac{\beta^2}{1-\beta^2}\right) - a_i\beta^2 + b'_i \right] \tag{5}$$

with $b'_i = b_i - 2a_i \ln\alpha$.

Table 2 shows the Bethe coefficients for Hydrogen, Helium and Neon.

	a_i	b'_i
H	0.156	8.115
He	0.174	7.653
Ne	0.456	18.17

Table 2: Bethe coefficients for Hydrogen, Helium and Neon [11, table II].

Figure 5 shows the total ionization cross sections of Hydrogen, Helium and Neon during the energy ramp and indicates that the obtained signal strength - in form of ionized electrons - remains approximately constant.

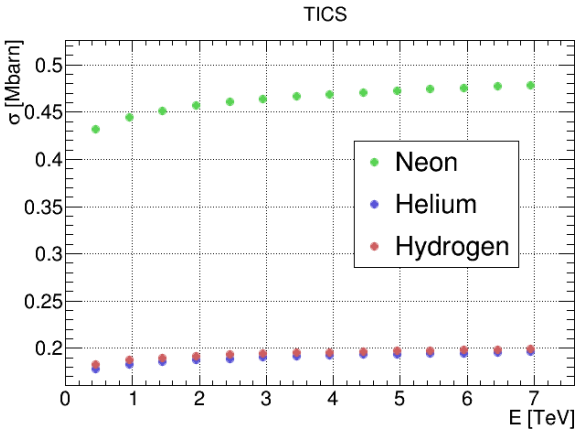

Figure 5: Total ionization cross sections for Hydrogen, Helium and Neon after equation (5) during the energy ramp. The Bethe coefficients are taken from table 2.

4.2.2. Voitkiv approach

Voitkiv et al. [16] did a fully analytical quantum mechanical approach in order to obtain the differential cross sections for Hydrogen. The electron movement is described by the non-relativistic Schroedinger equation (in consideration of soft emitted electrons) and the use of Coulomb continuum wave functions. The interaction with the projectile is described by an interaction term compound of its scalar and vector field to first order (spin effects are neglected).

The results are expanded to Helium by the introduction of an effective nucleus charge seen by the electrons. However this concept becomes disputable when going to more complex atomic structures, also because it does not account for ionization from different shells. The double differential cross section for Helium is given by [16, eq.(38)]:

$$\begin{aligned}\frac{d^2\sigma_{He}^{(+1)}}{dEd\Omega} = 2\cdot 2^8 \frac{Z^2}{v^2 Z_t^4} \frac{1}{\left(1+\frac{2E}{Z_t^2}\right)^5} \frac{\exp\left(-\frac{4\arctan\sqrt{\frac{2E}{Z_t^2}}}{\sqrt{\frac{2E}{Z_t^2}}}\right)}{1-\exp\left(\frac{2\pi}{\sqrt{\frac{2E}{Z_t^2}}}\right)} \\ \times \left[\sin^2\theta\cdot\ln\eta_{He} + \frac{\cos^2\theta}{\gamma^2} - 0.5\sin^2\theta \right. \\ \left. + \frac{8\sqrt{2E}}{v}\cos\theta\cdot\left[1-\frac{v^2}{2c^2}\right]\sin^2\theta\ln\eta_{He} + \frac{2ZZ_t}{v^2\gamma^2}\cos\theta\ln^2\eta_{He}\right] \end{aligned} \tag{6}$$

where Z is the charge of the projectile, a_0 the Bohr radius, Z_t the effective charge of Helium, η_{He} a material dependent coefficient, γ the relativistic factor and v the velocity of the projectile. The leading factor 2 corresponds to the two electrons in the 1s-shell of Helium. The cross section is given in atomic units.

Voitkiv et al. discuss that for Helium the calculated cross sections deviate from experimental

ones. Using $Z_t = 1.5$ the shape of the differential cross sections shows good agreement but because the total ionization cross section deviates they introduced an additional scaling factor which resolved this issue at a value of 1.9. Therefore we can expect deviation of this theoretical approach for Neon (only by use of a different effective charge) from real cross sections (for which, to our knowledge, no experimental data exists). However we are only interested in the differential cross sections and therefore an optimal value for the effective charge should be established. We used the theoretical value $Z_t = 5.758$ as presented in [4]. In addition a parameter scan has been performed but the results did not indicate a clear value for Z_t (see appendix A). Thus the results were dismissed, especially because of the poor quality of the available IPM data.

Figure 6 shows the double differential cross section calculated with an effective charge of $Z_t = 5.758$. It shows that transverse scattering is strongly favoured in accordance with the fact that the electric field of the beam is mostly transversal due to relativistic effects. Most of the electrons are soft emitted, the peak of the cross section is around 12 eV while electrons produced at rest almost do not occur.

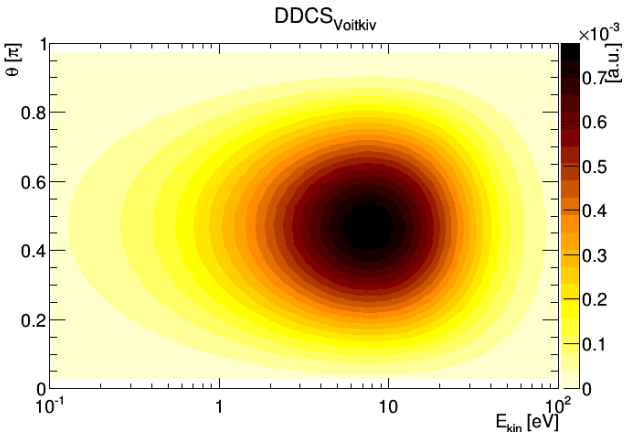

Figure 6: Double differential cross section for Neon after equation (6) for protons at 4 TeV and an effective charge of $Z_t = 5.758$. The cross section is given in atomic units.

4.2.3. Comparison

The Bethe approximation accounts for ionization from different shells by the introduction of the dipole oscillator strength. However the description of slow ionized electrons with a plane wave is a rough approximation and this low energy domain is expected to contribute the most for relativistic collisions. Also the assumption of independence of the dipole oscillator strengths from the energy of the incident particle is problematic when considering large energy ranges for the projectiles. Experimental data for the dipole oscillator strengths are not available for proton energies as in the LHC.

The Voitkiv approach uses the non-relativistic Schroedinger equation for the electron movement and therefore is expected to give reliable results for the low energy domain. However an analytical expression can only be derived for Hydrogen which was successfully extended to Helium by the introduction of an effective charge. Because Neon gas is used in the LHC-IPMs the concept of single electrons in the potential of an effective charge is disputable. However ionization will mostly occur from the outermost shell and therefore the use of an according effective charge allows for a reasonable description.

Figure 7 shows the comparison of the single differential cross sections after Bethe and Voitkiv. One can observe that the cross section after Voitkiv features slightly higher electron energies.

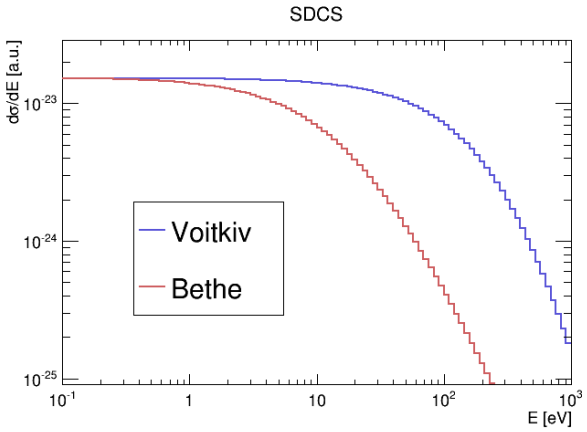

Figure 7: Single differential cross sections after Bethe and Voitkiv for protons at 4 TeV. The cross sections are scaled for comparison.

For the following investigations the double differential cross section after Voitkiv with an effective charge of $Z_t = 5.758$ was used.

4.2.4. Influence of the bunch electric field on the cross section

An important prerequisite for IPMs is that the electron distribution emerging from the ionization process is proportional to the initial proton distribution. In that case one will record a profile which is actually proportional to the beam profile (without any effects of distortion). Besides a homogeneous gas density in the ionization chamber another important requirement is that the ionization probability does not change along the transverse beam

profile under the influence of the bunch electric field (that is that the Stark effect must not affect the ionization process). Otherwise the emerging electron distribution would not match the actual beam profile but it would be modified according to the bunch electric field which itself depends on the beam size.

The scalar polarizability of Neon is about $4.41 \cdot 10^{-41}\,\mathrm{C^2m^2J^{-1}}$. The bunch electric fields for different energies during the ramp are shown in Fig. 8. The maximum is around $3\,\mathrm{MVm^{-1}}$ and hence the energy shift due to the quadratic Stark effect is calculated as:

$$\Delta B = \frac{\alpha}{2} \cdot E^2 \qquad \Rightarrow \qquad \Delta B \approx 1.23 \cdot 10^{-9}\,\mathrm{eV} \tag{7}$$

Because it is in the order of nano electronvolt its influence is not relevant for the ionization process.

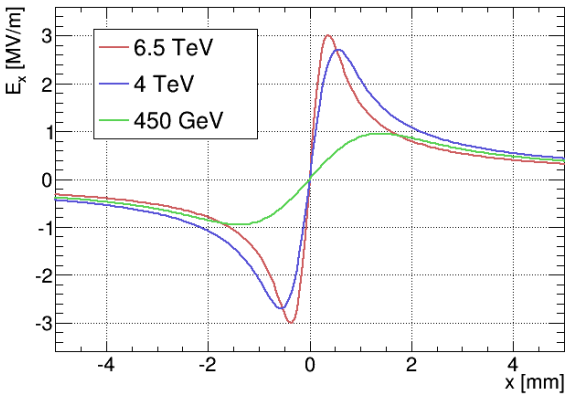

Figure 8: Bunch electric field along x for different beam energies (compare table 1).

5. Profile distortion

The space charge effects lead to heavily distorted profiles for beam energies above injection as shown in Fig. 9. Here *initial* denotes the situation immediately after ionization without suffering from any space charge effects while *final* means the situation at the detector after interaction with space charge. The beam parameters for the presented cases are given in table 1. One can observe that the tails of the profiles basically stay the same while most of the distortion is visible in the center of the profiles. This is due to the fact that the increase of gyroradii depends on the distance from the bunch center and is negligible at the outermost parts of the profile (compare Fig. 11, left). The increase of gyroradii along the transverse beam profile follows approximately the shape of the electric field of a bunch [15, Fig.9].

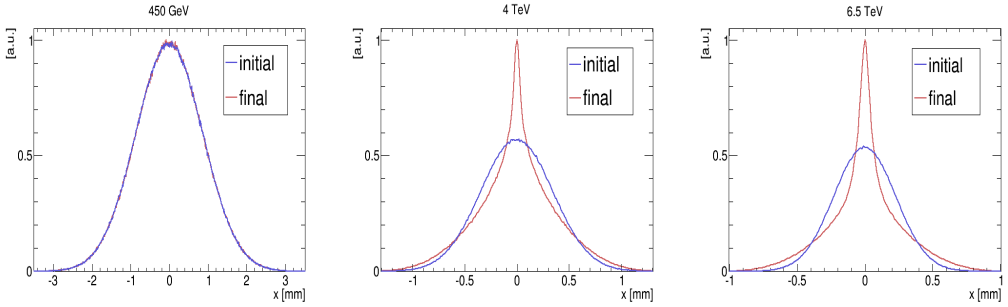

Figure 9: Profile distortion due to interaction with space charge for different beam energies.

Figure 10 shows the x-trace-space configuration of electrons after space charge interaction. One can observe that while the spatial distribution of electrons shrinks (according to the size of the beam profile) their velocities increase (corresponding to larger gyroradii). The plots show the variable velocities of electrons with respect to x while the gyroradii depend on the constant velocities in the x-z-plane $\left(v_x^2 + v_z^2\right)^{1/2}$. Because the displacement of electrons arises from their gyration parallel to the detector the velocities at the edges of the profiles are zero (electrons are "turning back"). Figure 10 as well as Fig. 11 (right) shows that the maximum increase of gyroradii is slightly less for the 6.5 TeV case than for the 4 TeV case although the bunch electric field is stronger for 6.5 TeV (compare Fig. 8). This is because for higher energies the beam size shrinks and thus the electrons are ionized accordingly closer to the bunch center. The increase of gyration arises from the acceleration of electrons towards the bunch center but because the electrons are created closer to the bunch center their path of acceleration decreases resulting in less increased gyroradii. Although the strength of the bunch electric field increases the electrons are positioned closer to the bunch to such an extent that the resulting maximum gyroradius increase due to acceleration is less.

However Fig. 9 shows that the distortion is stronger for the 6.5 TeV case than for the 4 TeV case. This is because the effect of gyroradii on the profile distortion increases with decreasing beam size. Figure 11 (right) shows that the final gyroradius distributions are almost the same for both cases but the same final gyroradii have a stronger effect on the distortion of a profile that is more narrow. That is the gyration of electrons actually causes the distortion, however the extent of distortion is determined by the final gyroradius distribution of electrons as well as the initial profile width, that is the beam size.

Regarding the emerging electron distribution which moves towards the detector as a secondary beam one can calculate its emittance from the phase space plots in Fig. 10. However this secondary emittance turns out not to be constant, neither when scaled with the (primary) beam energy, and thus could not be brought in relation with the (primary) beam emittance. Otherwise a measurement of the secondary electron beam emittance could be a possible indicator for the actual (primary) beam emittance.

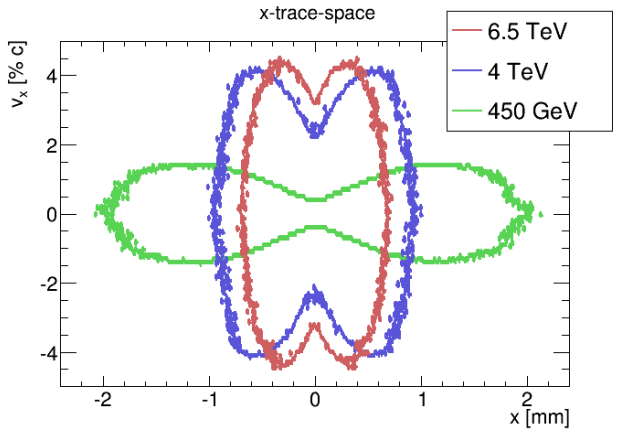

Figure 10: Trace space plots (95% surface) after space charge interaction for different beam energies. The binning is 10 μm for x and 0.1 %c for v_x.

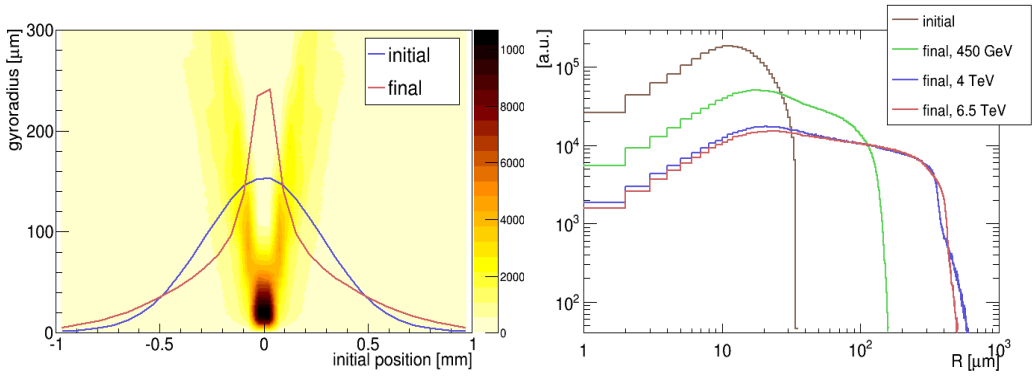

Figure 11: Impact of space charge on the gyroradius distribution of electrons. Left: Correlation between final gyroradii and initial x-position for the 6.5 TeV case. Right: Comparison of initial and final gyroradius distributions.

5.1. Mechanisms of distortion

The electrons in the LHC-IPMs perform many revolutions until they reach the detector. Simple estimations yield a time of flight of around 3.2 ns and the gyro-frequency of electrons is about 35 GHz for a magnetic field strength of 0.2 T. Thus the number of revolutions performed until the electrons reach the detector is about 100 and therefore the electrons will actually perform a long-term gyration. After being extracted from the bunch region

by the external electric field the electrons perform a purely circular movement in presence of the external magnetic field in the x-z-plane at detector level (the influence of the bunch electric field is negligible at this level). This gyration leads to probabilities for electrons to be detected at any of the bins (camera pixels) within their gyration range - not only at the one which corresponds to the position of their gyration centers - and thus to a distortion of the registered profile. The possibility to resolve the electron positions is generally limited by the binning of the acquisition system. In case of the LHC-IPMs the optical system leads to an effective pixel size of around $110 \times 110\,\mu m^2$ [14], for the simulations a binning of $10\,\mu m$ with respect to x was used in order to avoid resolution problems and to concentrate on the actual profile distortion. The final profile is obtained by integrating the signal over all pixels along z. Figure 12 shows a visualization of the gyration and the according displacement on neighbouring bins as well as the effect of those displacements on a Gaussian profile.

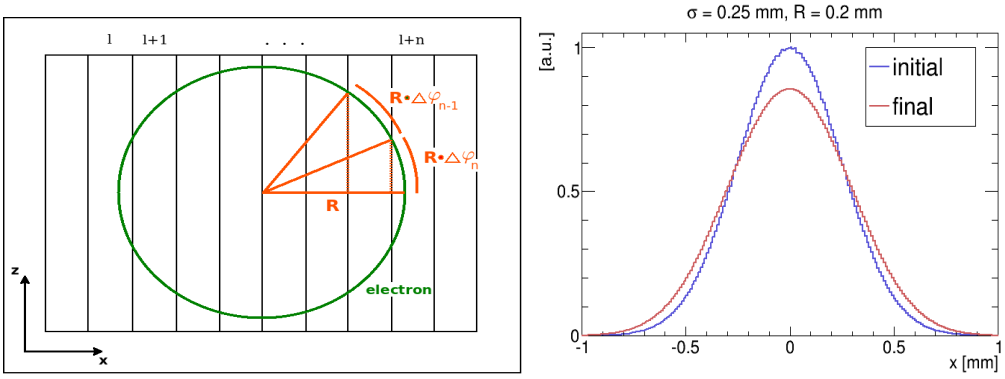

Figure 12: Mechanism of profile distortion due to spiraling of electrons. Left: Visualization of the gyration of electrons above the detector; for the sake of clarity the binning with respect to z has been spared. Right: Profile distortion due to a uniform gyration of electrons with gyroradii $R = 0.2\,\text{mm}$.

5.1.1. Probability of displacement

The probability p_i that an electron is detected on a certain bin i within its gyration range $2R$ is proportional to the time that the electron spends above the respective bin and because of its constant velocity in the x-z-plane it is proportional to the length of the arc "lying" over the respective bin (see Fig. 12)

$$p_i = \frac{\Delta\varphi_i}{\pi} = \frac{\varphi_i - \varphi_{i+1}}{\pi} = \frac{1}{\pi} \cdot \left[\arccos\left(\frac{\beta_i - x_0}{R}\right) - \arccos\left(\frac{\beta_{i+1} - x_0}{R}\right) \right] \tag{8}$$

where β_i denotes the lower edge of bin i and x_0 the gyration center of the electron with respect to x. If the gyration spans from bin l over $n+1$ bins to bin $l+n$ then the boundary conditions $\varphi_l = \pi$ and $\varphi_{l+n} = 0$ apply.

Speaking of a "probability" in this context implies that while the electrons are gyrating in the x-z-plane the moment of detection is completely random. But in fact the moment of detection depends on the beam parameters and the initial positions and momenta of electrons. Suppose for example that all electrons are generated at the same initial position,

with the same initial momentum. Furthermore there shall be no beam and all electrons are moving in the same constant electric and magnetic field. Then they all describe a gyration in the x-z-plane while they are moving towards the detector. Although they are gyrating over multiple bins in the end all electrons will be registered on the same bin. In that case it would be incorrect to describe the distortion via equation (8). Because the movement of electrons and thus the moment of detection is deterministic it is important that they are initially uniformly distributed. The spatial distribution of electrons with respect to y is Gaussian but this is not essential. Instead it is important that the distribution of times-of-flight (the time an electron needs to reach the detector) is uniform or at least does not change perceptibly on a time interval of the length of the revolution time of an electron. To be valid for all components of the registered profile this must apply for all gyroradii. The gyro-frequency is given by:

$$\omega = \frac{qB}{m} \qquad \Leftrightarrow \qquad T_{\mathrm{rev}} = 2\pi \frac{m}{qB} \tag{9}$$

For a magnetic field of 0.2 T this yields $T_{\mathrm{rev}} = 0.18\,\mathrm{ns}$. Thus the time-of-flight distribution must be smooth on an interval of 0.18 ns for every gyroradius. Figure 13 shows such a distribution obtained from the simulation data for the 6.5 TeV case and indicates that the requirement is fulfilled. As one can observe electrons with smaller gyroradii tend to need less time to reach the detector than the ones with higher gyroradii do. This is because the greater the gyroradius of an electron is (emerging from an increase of gyration) the more it interacted with the bunch electric field before. This interaction also takes place in direction towards the detector and thus slows down the extraction of electrons.

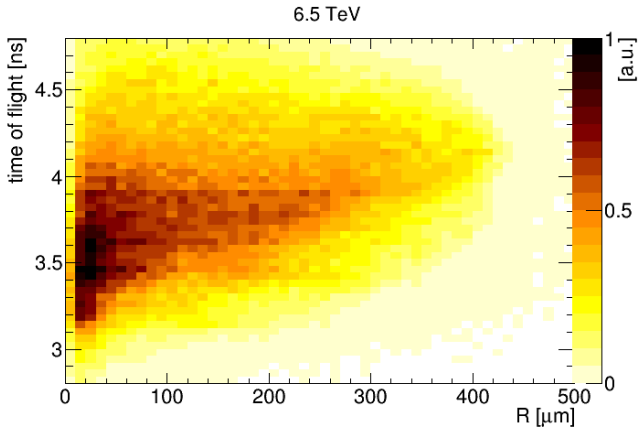

Figure 13: Time-of-flight distribution of electrons in dependency of their gyroradii. The binning is 0.04 ns for the time and 10 μm for the radius.

5.1.2. Shift of gyration center

As this model of displacement due to gyration applies at detector level where the electrons are not suffering from the bunch electric field it is important that the gyration centers of electrons at detector level do not differ from their production points with respect to x.

However such a deviation is already implied by the initial velocity distribution depending on the scattering angle θ. The kinematic equations of motion of an electron in a uniform magnetic field are (in the x-z-plane)

$$\begin{aligned} x(t) &= x_0 + \frac{v_{x0}}{\omega}\sin(\omega t) + \frac{v_{z0}}{\omega}\left[1-\cos(\omega t)\right] \\ z(t) &= z_0 - \frac{v_{x0}}{\omega}\left[1-\cos(\omega t)\right] + \frac{v_{z0}}{\omega}\sin(\omega t) \end{aligned} \tag{10}$$

with the synchrotron frequency $\omega = qBm^{-1}$ and

$$v_x = \sqrt{2Em^{-1}}\sin\theta$$

$$v_z = \sqrt{2Em^{-1}}\cos\theta$$

The initial velocities are determined by the initial kinetic energy and the scattering angle as described by the corresponding cross section. For transverse scattering ($\theta = \pi/2$) this yields:

$$\begin{aligned} x(t) &= x_0 + \frac{v_{x0}}{\omega}\sin(\omega t) \\ z(t) &= z_0 - 2\frac{v_{x0}}{\omega}\sin^2\left(\frac{\omega t}{2}\right) \end{aligned} \tag{11}$$

Equation (11) shows that a transversely scattered electron performs a periodic movement around x_0 while it deviates by $v_{x0}\omega^{-1}$ from its production point with respect to z. Because transverse scattering is preferred in the ionization process (compare section 4 and Fig. 6) most of the electrons will suffer only to minor extent from a displacement with respect to x as shown in Fig. 14 (the RMS of the displacement is about $10\,\mu m$). The same figure also shows the deviation of the gyration center from the production point after interaction with space charge, that is at detector level, which matches the initial distribution. As a collective plot this does not prove that there is no influence from the bunch electric field (the plot could be mirrored for example) however this has been verified by plotting the one-to-one correlation $dx_f - dx_i$ (which equals always to zero for a binning of $1\,\mu m$). Because of the simplicity of this plot it was spared.

In the end the independence of this gyration center shift from the beam size (and the beam electric field) is important. As long as the shift induced by the ionization process is known by availability of an appropriate cross section one can correct for its effect by applying a deconvolution where the corresponding point spread function is the shift probability with respect to x (compare Fig. 14; for deconvolution see section 5.2.2). For a Gaussian shift distribution one can also apply a correction in quadrature in order to account for this effect:

$$\sigma^2_{\text{original}} = \sigma^2_{\text{measured}} - \sigma^2_{\text{shift}}$$

However because the extent and thus the effect of the shift is small compared to the used binning and the extent of gyration of electrons, it is neglected in the following considerations.

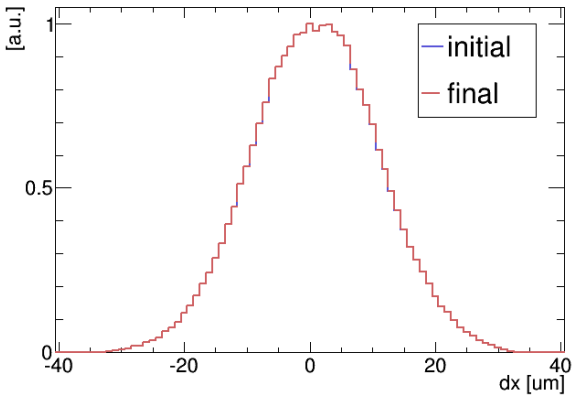

Figure 14: Deviation of the gyration centers of electrons at detector level from their production points with respect to x. The binning is $1\,\mu m$. The data was obtained for initial velocities corresponding to section 4.2.2.

5.2. Description of distortion

In case that a registered profile consists only of electrons with the same gyroradius one can restore the corresponding initial profile from the distorted one if the gyroradius is known. Using the above described mechanism of profile distortion one can establish formalisms in order to describe the distortion in dependency of the gyroradius and accordingly compute the distorted profile from the initial one and vice versa.

5.2.1. Distortion matrix

An arbitrary (linear) transformation of a profile P (consisting of N components) into a distorted profile P' can be described by the multiplication with a matrix that describes the way of distortion:

$$M \cdot P = P' \quad \Leftrightarrow \quad \sum_{j=1}^{N} M_{ij} P_j = P'_i \tag{12}$$

This system of equations can be solved for P in order to obtain the original profile.
The distortion matrix M is determined by the mechanisms discussed in 5.1 and equation (8) specifically

$$M_{ij} = \frac{1}{\pi} \cdot \left[\arccos\left(\frac{\beta_i - \gamma_j}{R} \right) - \arccos\left(\frac{\beta_{i+1} - \gamma_j}{R} \right) \right] \tag{13}$$

where γ_j denotes the center of bin j and β_i the lower edge of bin i. The matrix element M_{ij} describes the extent of displacement of electrons that are created above bin j onto bin i. This representation is valid under the assumption that all electrons produced within the range of a bin actually gyrate around its center which is an approximation but can be easily replaced by for example a uniform distribution of electrons over the respective bin. However the maximal deviation from this assumption is half a binsize which becomes negligible especially when the gyration spans over multiple bins.

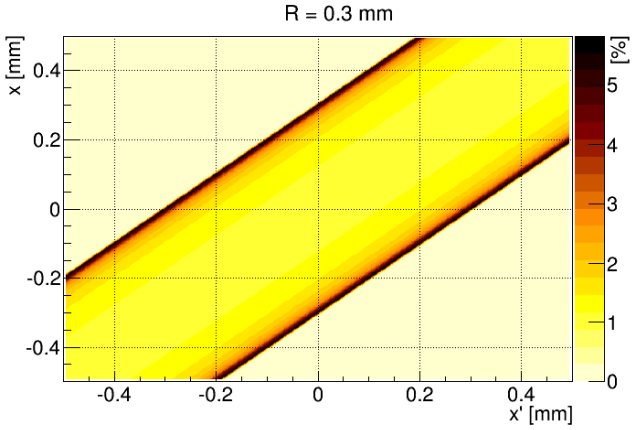

Figure 15: Visualization of the displacement of electrons on neighbouring bins. This is similar to the corresponding distortion matrix.

Figure 15 shows the displacement of electrons on neighbouring bins and thus visualizes the corresponding distortion matrix. The matrix is symmetric because the way of distortion only depends on the gyroradii but not on the initial positions of electrons.

In this representation the distortion matrix also describes a displacement emerging from bins where actually no electrons have been in the original profile. With knowledge of the width of the distorted profile and the extent of displacement (determined by the gyroradius of electrons) one can confine the width of the original profile and adapt the distortion matrix such that an iterative solution of the components of P is possible. Because the outermost parts of the distorted profile can only arise from electrons which gyrated around the outermost parts of the original profile one can determine their contribution and accordingly the contribution to all other bins within their gyration range. In a subsequent step one can do the same for the next bin towards the profile center by using the beforehand obtained knowledge of previous contributions. That way one can determine all components of the original profile going from its outermost parts to the innermost. Figure 16 visualizes the concept of this iterative reconstruction which can be realized for example in form of an adapted distortion matrix.

However in case of uncertainties regarding the knowledge of the gyroradius with which the original profile has been distorted solving this system of equations is rather error prone in form of an amplification of potential deviations for the input.

5.2.2. Convolution

The fact that the way of displacement (for a single gyroradius) does not depend on the initial positions of electrons but only on their gyroradius, that is it is the same for every part of the initial profile, gives rise to the idea of using point spread functions (PSF) in order to describe the distortion. In this context the distortion of the original profile P is described by the convolution with a corresponding point spread function denoted by ξ:

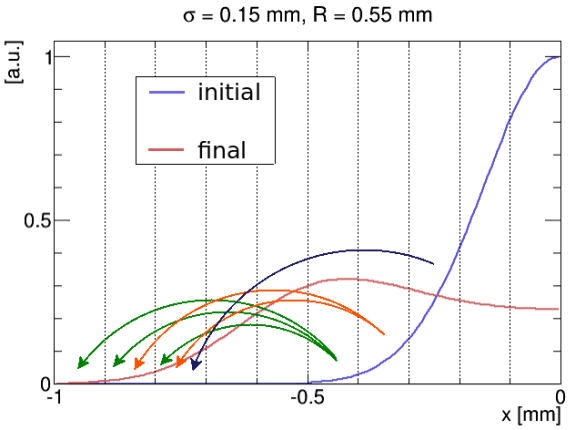

Figure 16: Visualization of the iterative reconstruction of the original profile for a known gyroradius.

$$P'_j = (P * \xi)_j = \sum_{k=-n/2}^{n/2} P_{j-k} \cdot \xi_k \tag{14}$$

This technique of describing a distortion which depends on external parameters via convolution with a corresponding point spread function is often used in other fields as for example optics where one wants to describe the blurring of a two-dimensional picture in dependency of the properties of the recording device.

In order to obtain the original profile from equation (14) one has to invert the process by applying a deconvolution algorithm.

In our case the point spread functions are calculated in a similar way to the (symmetric) distortion matrix that is described by equation (13). Again the way of displacement described by equation (8) is essential. The point spread functions describe to what extent the contribution of each component of the original profile will go over to their neighbouring components. Figure 17 shows point spread functions corresponding to different gyroradii.

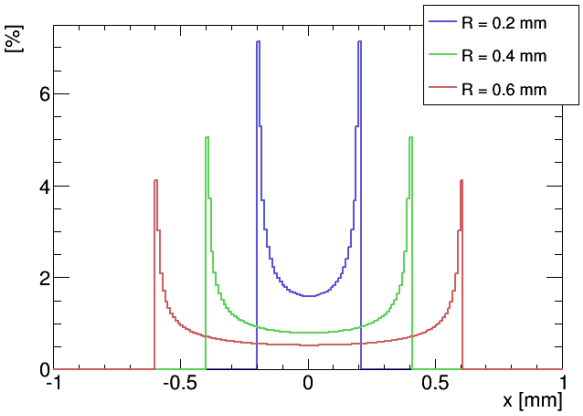

Figure 17: Point spread functions corresponding to different gyroradii.

6. Profile correction

The profile distortion arises mainly from the gyration of electrons which is increased by the interaction with the bunch electric field. This increase is non-uniform along the transverse beam profile (compare Fig. 11, left) and depends on the initial positions of electrons as well as on the beam parameters. For each position along the transverse profile electrons of various gyroradii are registered, determining the observed profile. Because the extent of distortion is depending on the gyroradii of electrons (compare equation (8)) the idea is to separate the electrons with respect to their gyroradii. Grouping electrons with similar gyroradii together allows to describe the distortion of those partial profiles with the formalisms discussed in section 5.2 and thus makes it possible to restore the corresponding initial profiles.

6.1. Electron sieve

Because an actual measurement of gyroradii is rather complicated the concept of an electron sieve is proposed in order to acquire the different partial profiles. Such a sieve could be realized in form of a disk with rectangular gaps of different widths in order to allow only electrons with gyroradii $R < R_i$ to pass where R_i is the half-width of gap i (see Fig. 18). The thickness of the sieve depends on the gyro-frequency ω of electrons and their velocities towards the detector. The requirement is that every electron performs at least one full revolution within a gap to ensure that it will be absorbed if its gyroradius is too large. That is the thickness must be at least $2\pi\bar{v}_y\omega^{-1}$ where $\bar{v}_y$ is the upper limit for electron velocities towards the detector. Simple estimations without the influence of the bunch field as well as the simulations yield final velocities $v_y \approx 0.09\,\mathrm{c}$ (see Fig. 19).

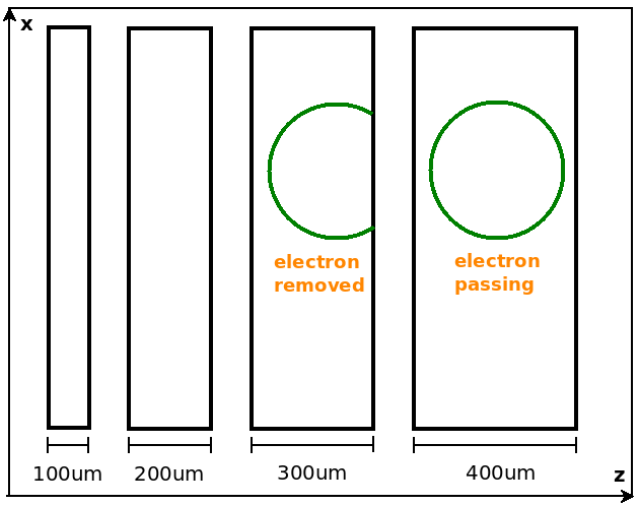

Figure 18: Sketch of an electron sieve with rectangular gaps. The electron on the right will pass through the sieve while the one on the left will be absorbed because its gyroradius is too large.

In addition it is important that the sieve is aligned perpendicular to the magnetic field lines because any tilt would change the effective widths of the gaps (as the electrons gyrate around the magnetic field lines and travel along them).

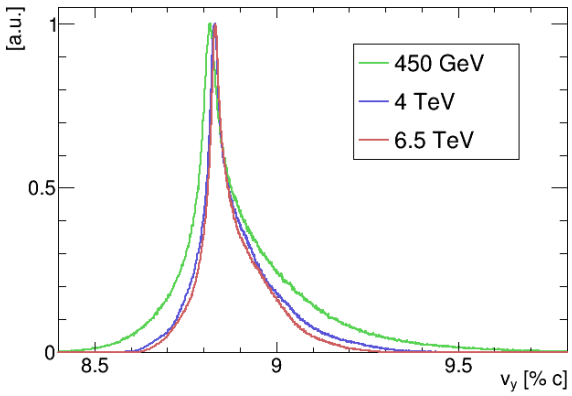

Figure 19: Electron velocities with respect to y at the moment of detection for different beam energies.

In the following we will consider a sieve with rectangular openings because they turn out to be the most practical. However other geometries for the sieve openings are possible, appendix C includes investigations on this topic.

6.1.1. Non-uniform transmission

Within the concept of such a sieve gap i will only record electrons with gyroradii in the interval $[0, R_i]$. The corresponding profile is denoted with $P_{[0,R_i]}$. In order to be able to compute all partial corrections (corresponding to different groups of gyroradii) one needs to separate the electrons in intervals $[R_i, R_{i+1}]$ (instead of $[0, R_{i+1}]$). The corresponding profiles are denoted with $P_{[R_i,R_{i+1}]}$. A first idea how to obtain those profiles would be to subtract two subsequent recorded profiles from each other:

$$P_{[R_i,R_{i+1}]} = P_{[0,R_{i+1}]} - P_{[0,R_i]} \tag{15}$$

However this only works if profile $P_{[0,R_{i+1}]}$ contains as many electrons within the range $[0, R_i]$ as $P_{[0,R_i]}$ does. The bunches will ionize the gas in the chamber along z everywhere to the same extent which results in an independence of the emerging profiles on z. The drifting of electrons along the beam does not play a role if the chamber in which the sieve is placed is large enough (as much larger as the farthest drift can be). In that case the emerging gyroradii are the same along z and thus the gaps will acquire more electrons with small gyroradii than ones with larger gyroradii for every position along x. In addition larger gaps will collect even more electrons of a certain gyroradius than smaller ones do. The amount of electrons collected is proportional to the length of the segment within a gap (with respect to z) on which the gyration center of an electron can be located without causing contact of the electron with the disk. Thus the amount of electrons collected by gap i is proportional to

$$T_{[0,R_i]} = -2R + 2R_i \tag{16}$$

where R_i is the half-width of gap i. Note that $T_{[0,R_i]}$ (in the following called *transmission*

function) denotes a proportionality to the number of electrons of a certain gyroradius that are collected by gap i, not the actual amount. Hence this quantity is used for comparison between different gaps. Because this proportionality depends always on the (full-)width of gaps ($2R_i$) and the diameter of gyration ($2R$) we substitute $R_i \equiv 2R_i$ and $R \equiv 2R$ for the sake of readability. Because we will not encounter any dependence on the radius itself (or the half-width of a gap) this will not affect the following considerations and if necessary we will replace the substitution with its original expression. Figure 20 shows transmission functions corresponding to different gap widths.

When speaking of contributions of electrons with different gyroradii throughout this section we do not refer to the actual underlying gyroradius distribution (which emerges from the space charge interaction, as shown in Fig. 11) but to the artificially introduced change in contribution which happens in addition by the use of an electron sieve.

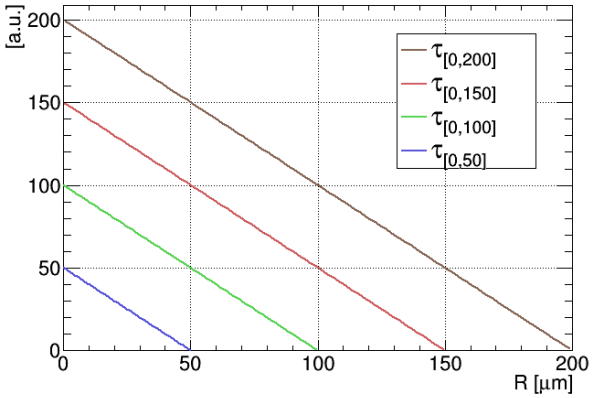

Figure 20: Plot of the different transmission functions for the example sieve of Fig. 18.

6.1.2. Acquisition of partial profiles

Following the previous considerations the subtraction performed in equation (15) will not completely remove the low gyration electrons in the interval $[0, R_i]$ from the profile $P_{[0,R_{i+1}]}$. Another idea how to account for this issue could be to scale the subtracted profile accordingly:

$$\begin{aligned} P_{[R_i,R_{i+1}]} &= P_{[0,R_{i+1}]} - \frac{R_{i+1}}{R_i} P_{[0,R_i]} \\ \Leftrightarrow \quad T_{[R_i,R_{i+1}]} &= T_{[0,R_{i+1}]} - \frac{R_{i+1}}{R_i} T_{[0,R_i]} \end{aligned} \tag{17}$$

However this subtraction is only complete for $R = 0$ while for $R > 0$ the remainder of the subtraction grows and the resulting profile still contains many electrons in the range of $[0, R_i]$. Choosing a different scaling will only shift the point where the subtraction is complete but will not change the fact that the profile still contains electrons on the whole interval. Using this method an effective transmission function after subtraction evaluates to:

$$T_{[R_i,R_{i+1}]} = \begin{cases} \left(\frac{R_{i+1}}{R_i} - 1\right) \cdot R & ,0 \leq R < R_i \\ \\ R_{i+1} - R & ,R_i \leq R < R_{i+1} \end{cases} \tag{18}$$

Figure 21 shows the transmission functions that emerge from this scaled subtraction.

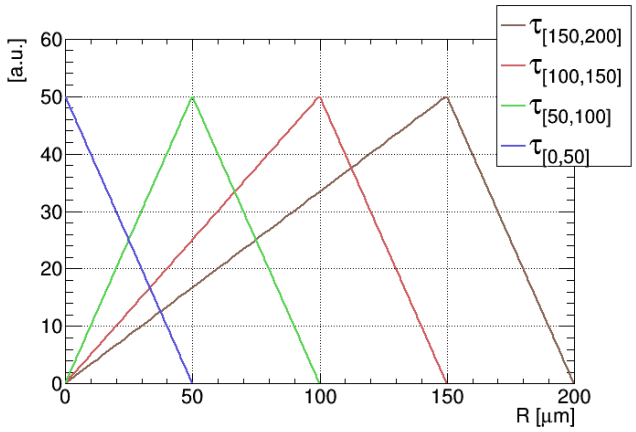

Figure 21: Transmission functions obtained by scaled subtraction of the preceding profile.

In order to estimate the quality of the emerging profiles (in terms of how well the profiles are limited to the essential intervals $[R_i, R_{i+1}]$) we will calculate the variance of transmission. The following equation turns out to be helpful for the calculations:

$$\int_0^{R_{i+1}} R^k \cdot T_{[R_i,R_{i+1}]} = \frac{R_{i+1}^{k+2} - R_i^{k+1} R_{i+1}}{(k+1)(k+2)} \tag{19}$$

From this we can easily calculate the mean gyroradius:

$$\begin{aligned} \overline{R}_{[R_i,R_{i+1}]} &= \frac{1}{\int_0^{R_{i+1}} T_{[R_i,R_{i+1}]} dR} \int_0^{R_{i+1}} R \cdot T_{[R_i,R_{i+1}]} dR \\ &= \frac{R_{i+1} + R_i}{3} \end{aligned} \tag{20}$$

Equation (20) implies that the mean gyroradius can be located even outside of the required interval $[R_i, R_{i+1}]$. This will accordingly lead to an increasing variance. The variance of transmission is given by:

$$\sigma^2_{[R_i,R_{i+1}]} = \frac{1}{\int_0^{R_{i+1}} T_{[R_i,R_{i+1}]}dR} \int_0^{R_{i+1}} (R-\overline{R})^2 T_{[R_i,R_{i+1}]}dR$$
$$= \frac{(R_{i+1}-R_i)^2 + R_{i+1}R_i}{18} \tag{21}$$

Thus the variance of a profile will increase with the width of its gap (in accordance with Fig. 21). A greater variance implies greater uncertainties in the description of distortion via convolution because the gyroradius with which the profile was distorted cannot be precisely determined and thus leads to greater deviations for the result of deconvolution. Another issue is that the partial corrections will have the same contributions of electrons of different gyroradii as the partial profiles that emerge from profile subtraction. Summing up the partial results in order to obtain the overall reconstructed profile will transfer those artificial non-uniform contributions to it and will accordingly cause a deviation from its actual Gaussian shape (which would be preserved in case of a uniform transmission for all gyroradii). Because the increase of gyroradii depends on the beam size and thus higher beam energies (and accordingly smaller beam sizes) require the sieve to cover a larger range of gyroradii this would define a limitation of this method in beam energy (as the variance of partial profiles increases with the acquisition of larger gyroradii and thus the quality of deconvolution accordingly decreases with increasing beam energy).

Improved subtraction

Instead of subtracting only the preceding profile from each registered profile it turns out to be more practical to subtract all preceding profiles - in a recursive manner - using appropriate weights for each. For the example set of gyroradii $\{50, 100, 150, 200\}$ this is:

$$\begin{aligned}
T_{[0,50]} &= -R + 50 \\
T_{[50,100]} &= T_{[0,100]} - \frac{T_{[0,100]}(0)}{T_{[0,50]}(0)} T_{[0,50]} \\
T_{[100,150]} &= T_{[0,150]} - \frac{T_{[0,150]}(0)}{T_{[0,50]}(0)} T_{[0,50]} - \frac{T_{[0,150]}(50)}{T_{[50,100]}(50)} T_{[50,100]} \\
T_{[150,200]} &= T_{[0,200]} - \frac{T_{[0,200]}(0)}{T_{[0,50]}(0)} T_{[0,50]} - \frac{T_{[0,200]}(50)}{T_{[50,100]}(50)} T_{[50,100]} \\
&\quad - \frac{T_{[0,200]}(100)}{T_{[100,150]}(100)} T_{[100,150]}
\end{aligned}$$

The weights of the subtracted profiles are chosen such that the subtraction is complete at their lower boundary R_i.

In the following we require the use of a regular sieve, that is the width of gap i can be written as a multiple of a basic width ΔR:

$$R_i = i \cdot \Delta R \tag{22}$$

Here ΔR specifies the binning of the sieve. Then the general case is given by

$$T_{[R_i,R_{i+1}]} = T_{[0,R_{i+1}]} - \sum_{j=0}^{i-1} \frac{T_{[0,R_i+1]}(R_j)}{T_{[R_j,R_{j+1}]}(R_j)} T_{[R_j,R_{j+1}]} \tag{23}$$

which evaluates to (for a proof see appendix B):

$$T_{[R_i,R_{i+1}]} = \begin{cases} 0 & ,0 \leq R < R_{i-1} \\ R - R_{i-1} & ,R_{i-1} \leq R < R_i \\ -R + R_{i+1} & ,R_i \leq R < R_{i+1} \end{cases} \tag{24}$$

Thus every transmission function equals to zero on the interval $[0, R_{i-1}]$ and is non-zero only on the interval $[R_{i-1}, R_{i+1}]$. Every transmission function has a triangular shape with a maximum value of ΔR as shown in Fig. 22.

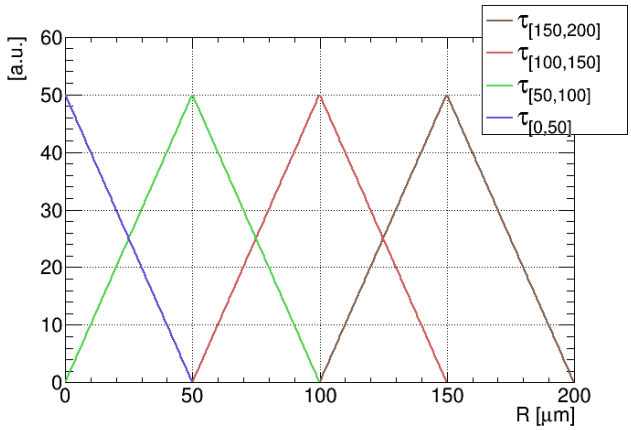

Figure 22: Transmission functions obtained by recursive subtraction of all preceding profiles.

Again we are interested in the variance of the resulting transmission in order to estimate the quality of the corresponding profiles. We will use the following equation:

$$\int_0^{R_{i+1}} R^k \cdot T_{[R_i,R_{i+1}]} = \frac{(\Delta R)^{k+2}}{(k+1)(k+2)} \left[(i+1)^{k+2} + (i-1)^{k+2} - 2i^{k+2}\right] \tag{25}$$

The mean gyroradius therefore results as

$$\overline{R}_{[R_i,R_{i+1}]} = \frac{1}{\int_0^{R_{i+1}} T_{[R_i,R_{i+1}]} dR} \int_0^{R_{i+1}} R \cdot T_{[R_i,R_{i+1}]} dR = i\Delta R \tag{26}$$

which meets our expectations as the function has a symmetric shape around R_i.

The variance is calculated as:

$$\sigma^2_{[R_i,R_{i+1}]} = \frac{1}{\int_0^{R_{i+1}} T_{[R_i,R_{i+1}]} dR} \int_0^{R_{i+1}} (R - \overline{R}_{[R_i,R_{i+1}]})^2 \cdot T_{[R_i,R_{i+1}]} dR = \frac{\Delta R^2}{6} \tag{27}$$

The important thing to note here is that the variance does not depend on the size of the sieve but it depends only on its binning ΔR (we could have expected that as with increasing R_i the transmission functions are only shifted with respect to the gyroradius but they do not change their shape). Thus there is no limitation in beam energy for this method. The only limitation is the binning of the sieve. One could expect again that the non-uniformity in transmission, which is reflected in the reconstructed partial profiles, will cause a deviation from the Gaussian shape for the overall profile but this is almost not the case. Equation (24) and Fig. 22 show that the two different non-zero parts of two subsequent transmission functions are complementary and sum up to ΔR for every gyroradius. Only the second part of the last transmission function has no complement but as shown in Fig. 23 the contribution of the last partial profile (corresponding to the highest gyroradii) is very small and thus its contribution is negligible for the shape of the overall reconstructed profile. Thus the reconstructed profile - emerging from summing up all partial results - only differs by a scaling factor from the original one (that is not ΔR because the transmission functions only indicate a proportionality to transmission but not its actual value). However a scaling factor does not change the variance and the width of the resulting profile. Therefore the only aspect which is affected by the binning of the sieve is the quality of the reconstructed partial results which is determined by how precisely the distortion of each partial profile can be described via convolution.

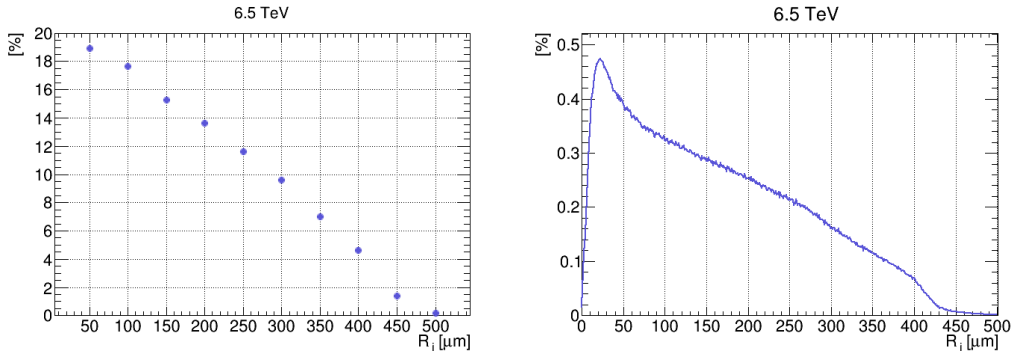

Figure 23: Percentage of electrons of different gyroradii to the final electron distribution. Left: Binning is 50 μm; Right: Binning is 1 μm.

6.2. Binning of gyroradii

In order to obtain the partial profiles corresponding to different gyroradii one has to choose a certain binning of the sieve with respect to the gyroradii which determines how electrons are grouped together to partial profiles. That means that instead of profiles corresponding to a

single, exact gyroradius one obtains profiles corresponding to certain intervals of gyroradii. Because the intrinsic gyroradius distribution of each interval (that is the shape of the profiles for the different intrinsic gyroradii, compare Fig. 11) is unknown the description of profile distortion via convolution will suffer from uncertainties which are increasing with the sizes of the intervals. Given a profile which contains electrons of multiple gyroradii the description of distortion via convolution becomes inexact and the question arises which point spread functions should be used in order to describe the distortion of the (combined) initial profiles in an optimal way.

An idea for the choice of the point spread function would be to choose a smaller, intrinsic binning for each interval and to use a weighted sum of point spread functions that correspond to this smaller binning (that is possible because the point spread functions are obtained from analytical considerations and thus are available for arbitrary binnings).

However the description of the distortion of a collective profile with a collective point spread function introduces an error in form of cross terms including the convolution of intrinsic profiles with point spread functions that correspond to different gyroradii.

Suppose a distorted profile was obtained at a certain binning, denoted by P', and consists of intrinsic profiles that are related to a smaller (non-resolvable) binning, denoted with P'_i. Those intrinsic profiles can be described by the convolution of their original counterparts, denoted by P_i, with the corresponding point spread functions denoted by ξ_i. This yields:

$$P' = \sum_i P'_i = \sum_i P_i * \xi_i \stackrel{!}{=} \tilde{P} * \xi^w \tag{28}$$

We claim the last equality because we want to describe the distortion in the collective profile P' with a point spread function ξ^w. In case that the description is exact the resulting profile $\tilde{P}$ equals the original profile P. However if the description is not exact then the deconvolution will yield a result that deviates from the original profile. The point spread function ξ^w which is used for deconvolution is the weighted sum of intrinsic point spread functions with arbitrary weights λ_i:

$$\xi^w = \lambda^{-1} \sum_i \lambda_i \xi_i \quad \text{, where } \lambda = \sum_i \lambda_i \tag{29}$$

A convolution of the original profile with this point spread function yields:

$$\begin{aligned} P * \xi^w &= \left[\sum_i P_i\right] * \left[\lambda^{-1} \sum_j \lambda_j \xi_j\right] \\ &= \sum_i P_i * \xi_i + \underbrace{\lambda^{-1} \cdot \left[\sum_{i \neq j} P_i * \lambda_j \xi_j - \sum_j (\lambda - \lambda_j) P_j * \xi_j\right]}_{=:H} \\ &= P' + H \end{aligned} \tag{30}$$

Comparison with equation (28) shows that the result does not equal the distorted profile P' because of the additional error term H. Deconvolution of the distorted profile P' with the point spread function ξ^w will accordingly yield a result which is different from the original

profile ($\tilde{P} \neq P$). The deviation is given by the error term H which contains convolutions of the intrinsic (non-resolvable) profiles P_i and thus cannot be simply added to the distorted profile in order to obtain an exact solution. However we are free in the choice of the point spread function which is used for deconvolution and thus we can try to choose it in such a way that the error term H becomes minimal. For that purpose we assume that the intervals are small enough so that the shape of the intrinsic profiles does not change markedly on each interval (that is their shape is approximately constant for each interval) although they may have different contributions μ_i (arising from the non-uniform transmission through the sieve). Then we can describe the intrinsic profiles with a common shape Q and variable contributions μ_i:

$$P_i = \mu_i \cdot Q \quad \text{and} \quad \mu = \sum_i \mu_i \tag{31}$$

Thus the error term evaluates to:

$$\lambda \cdot H = \sum_j (\mu - \mu_j) \cdot Q * \lambda_j \xi_j - \sum_j (\lambda - \lambda_j)\, \mu_j \cdot Q * \xi_j \tag{32}$$

If we choose the λ_j such that

$$\frac{\lambda - \lambda_j}{\lambda_j} = \frac{\mu - \mu_j}{\mu_j} \tag{33}$$

then the error term equals to zero (under the assumption that the intrinsic profiles P_i have the same shape for each interval). This relation implies that the weights equal the contributions of the partial profiles ($\lambda_j = \mu_j$).

One should keep in mind that the uniform shape of the intrinsic profiles for each interval is a strong assumption and does not only imply the smoothness of one parameter but of every part of the profiles and therefore a small invalidation might cause strong deviations for any results which are deduced under this assumption. Figure 24 shows the quality of the uniformity assumption for different interval sizes. For each size it shows best agreement for the profiles corresponding to intermediate gyroradii while it is worse for extremal gyroradii. Going to larger interval sizes decreases the quality of the assumption.

In order to obtain the weights for the intrinsic point spread functions one needs to specify the contributions of the different intrinsic profiles. On the one hand this is determined by the transmission through the sieve, but on the other hand this effect takes place in addition to the actual underlying contributions of different gyroradii (compare Fig. 11). Figure 23 shows the contributions of partial and intrinsic profiles and indicates that the change is small for interval sizes up to $50\,\mu m$. Because the contributions introduced by the non-uniform transmission of the sieve are predominant and because the underlying contributions are actually not available one can go with the assumption that the actual intrinsic contributions are constant on each interval and thus only consider the non-uniform transmission. Alternatively one could measure the contributions of subsequent partial profiles in order to interpolate their intrinsic contributions to be used together with the non-uniform transmission in order to obtain more precise results.

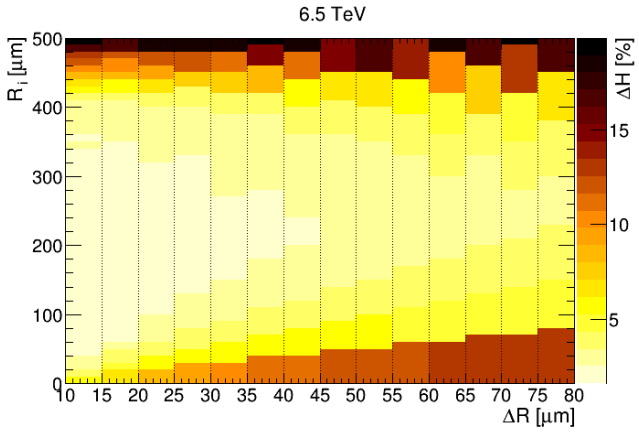

Figure 24: Quality of the assumption that the intrinsic profiles of each interval are uniform. The binning is $5\,\mu m$ for ΔR and $1\,\mu m$ for the intrinsic profiles. The total range covered along R is always $[0, 500]\,\mu m$. ΔH is the root mean square of the difference between the first and the last profile of each interval and is indicated on the full size of the respective interval.

6.3. Performance with simulation data

A preliminary study of the following investigations has already been presented in [15]. As a first step we investigate whether the model of convolution and deconvolution together with the point spread functions defined in section 5.2.2 - based on the model of displacement presented in section 5.1 - actually allows for a reconstruction of the partial profiles. For this purpose we firstly neglect the effect of non-uniform transmission in order to investigate only the effect of binning of gyroradii (in section 6.3.1). In a second step we will introduce the non-uniform transmission as obtained for equation (24) (in section 6.3.2). For the further investigations the simulation data for the 6.5 TeV case was used (compare table 1) together with various sieve binnings. All binnings cover the same range $[0, 500]\,\mu m$ and the interval sizes range from $10\,\mu m$ to $75\,\mu m$. For every electron its position and velocity of the moment it was created and the moment it was detected can be accessed. In addition the initial and final values can be mapped to each other. Thus we are directly able to determine the gyroradius of each electron by use of its parallel momentum:

$$R = \frac{\sqrt{p_x^2 + p_z^2}}{qB} \tag{34}$$

We use the initial profiles containing only electrons that will gyrate with the same radius at detector level later, that is P_{initial} for all R_{final}, as well as the profiles for the final positions, P_{final} for all R_{final}. The partial corrections are computed from the different P_{final} and are compared against the corresponding initial partial profiles P_{initial}.

A version of the Gold deconvolution algorithm, implemented in the TSpectrum class of the ROOT library [12], was used in order to obtain the following results.

6.3.1. Performance for uniform transmission

For the following investigations the transmission through the sieve will not be taken into account in order to study only the effect of gyroradius binning on the results of the method. This means that the underlying gyroradius distribution, emerging from the space charge interaction, is not altered.

Point spread functions with uniform weights

Under the assumption that the intrinsic profiles are uniform on each interval and in addition that their underlying contributions are the same on each interval all weights can be set to one according to equation (33).

The results obtained by use of the corresponding point spread functions generally show oscillations around the original profiles whose extent depends on the size of the intervals (see Fig. 25, 26, 27, 28). Although the reconstructed profiles show deviations from the original ones they restore their basic properties well. Figure 25 shows the deconvolution result for two different partial profiles obtained for an interval size of 50 μm. The oscillations are clearly visible but it is also obvious that the results follow the shape of the original profiles as well as they reflect their basic properties like the double peak and the central minimum.

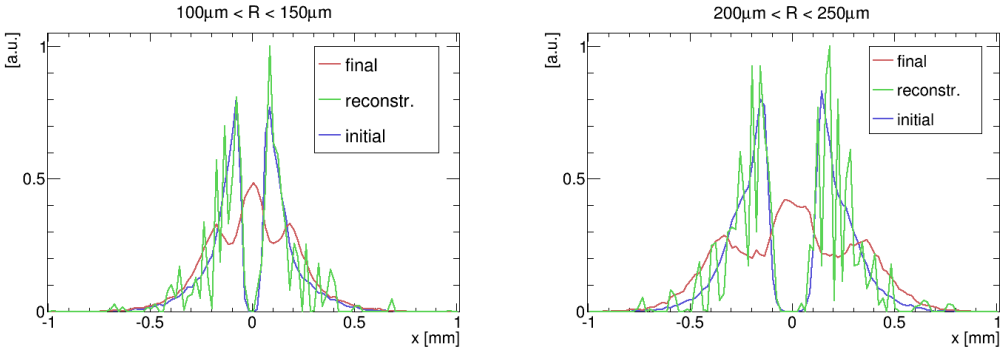

Figure 25: Reconstruction of two partial profiles. A uniformly weighted point spread function was used.

Oscillations of the reconstructed profile can be observed for every partial result and they are accordingly reflected in the overall result which is obtained by summing up all partial ones. The oscillations are periodic in such a way that a Gaussian fit nearly always converges well to the original profile as shown in Fig. 26. For the fit the procedure implemented in the TH1 class of the ROOT library was used together with the Loglikelihood method [12].

In order to investigate the effect of binning of gyroradii on the deconvolution results in form of oscillations of the reconstructed profiles the method has been performed for various interval sizes. The results for an interval size of 25 μm show clearly better accordance with the original profiles, especially the overall reconstructed profile contains only minor oscillations (see Fig. 27). For an interval size of 10 μm the profiles are restored even better, the overall profile contains almost no oscillations and matches the original one very well (see Fig. 28). Figure 29 shows the quality of the overall reconstruction in dependency of the used interval size. The quality clearly improves when using smaller intervals.

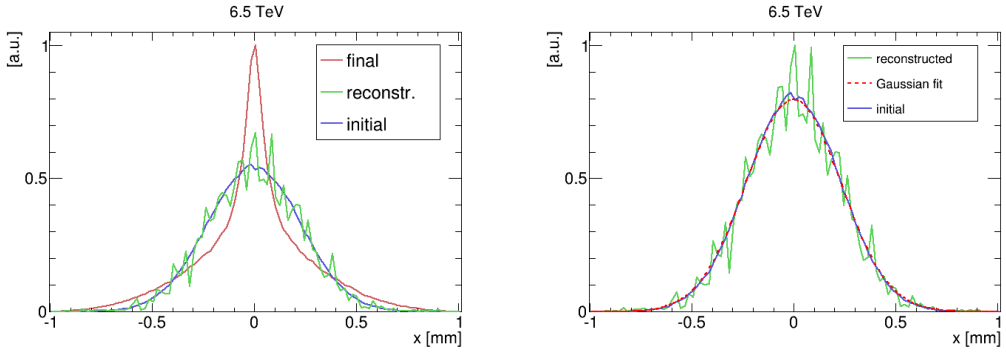

Figure 26: Reconstruction of the beam profile for a gyroradius binning of 50 μm. A uniformly weighted point spread function was used. The result is fitted with a Gaussian shape.

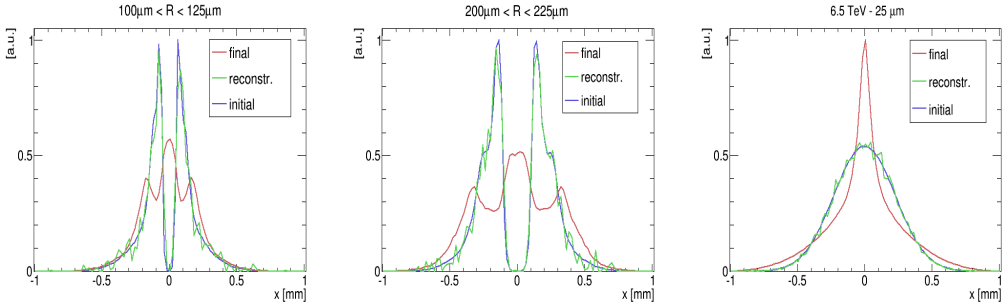

Figure 27: Reconstruction of the beam profile for a gyroradius binning of 25 μm. A uniformly weighted point spread function was used.

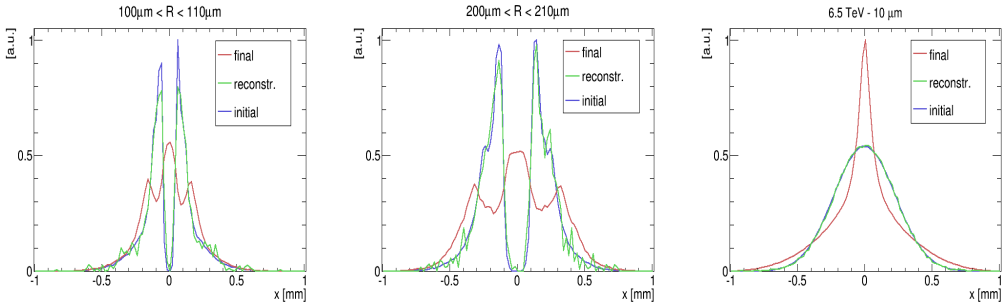

Figure 28: Reconstruction of the beam profile for a gyroradius binning of 10 μm. A uniformly weighted point spread function was used.

The sample size of the partial profiles has been estimated not to play a role for the quality of the deconvolution results, one obtains similar oscillations when using ten times more electrons, only their periodicity becomes slightly more obvious.

Point spread functions with interpolated weights

Alternatively to the assumption of uniform intrinsic contributions for each interval one can use the information of the contribution of subsequent registered profiles and accordingly

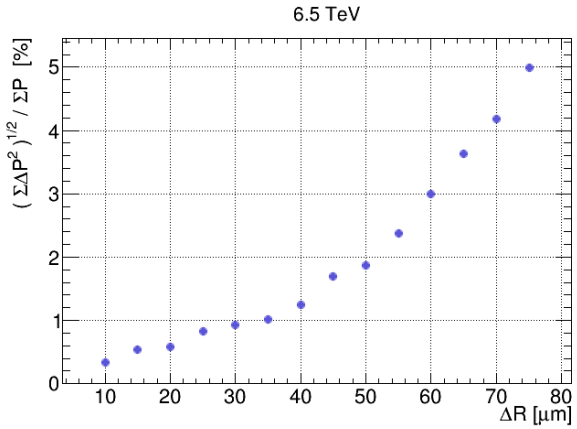

Figure 29: Deviation of the reconstructed profile from the original beam profile for different binnings of the sieve. A uniformly weighted point spread function was used.

interpolate the contributions of their intrinsic profiles (compare Fig. 23). Again equation (33) defines the appropriate weights for the point spread functions. A linear interpolation was used for the following results.

The results in Fig. 30 show slightly less oscillations than the ones in Fig. 25 and 26, however Fig. 31 shows that the results do not obviously improve in quality compared to the ones for uniform weights (compare Fig. 29). This is because the contributions of the intrinsic profiles of each interval change - especially for small interval sizes - only slightly, as shown in Fig. 23. Thus the used weights for the point spread functions also differ only to minor extent from each other, according to equation (33).

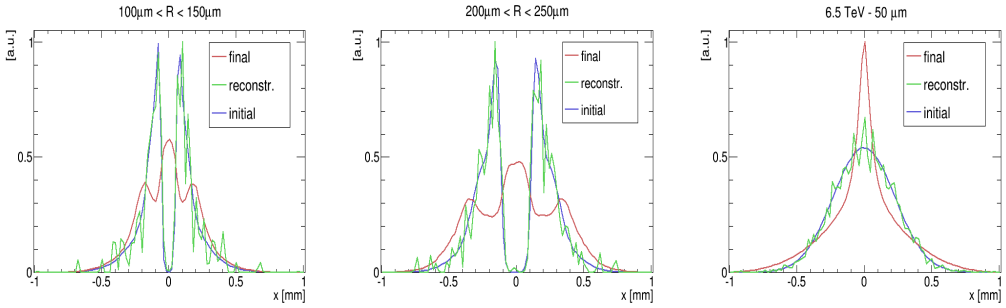

Figure 30: Reconstruction of the beam profile for binning of 50 μm. A weighted point spread function with weights obtained after equation (33) was used.

Single point spread functions

Alternatively to a weighted sum of point spread functions one can use a single (intrinsic) point spread function which corresponds to a gyroradius within the respective interval. In fact this is a special case for a weighted point spread function for which all weights but one are set to zero. Similarly to equation (30) one obtains:

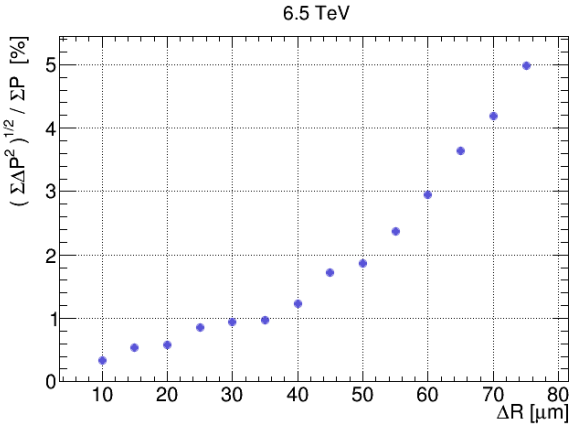

Figure 31: Deviation of the reconstructed profile from the original beam profile for different binnings of the sieve. A weighted point spread function with weights obtained after equation (33) was used.

$$P * \xi^w = \left[\sum_i P_i\right] * \xi_k = P' + \underbrace{\sum_i P_i * (\xi_k - \xi_i)}_{=:H} \tag{35}$$

Again the deconvolution will yield a deviating result depending on the additional error term H. In order to obtain best possible results H should be as small as possible. Its component for $i = k$ is zero and the others increase with $|k - i|$. Therefore the usage of the point spread function which corresponds to the arithmetic mean of the contributions within each interval is obvious. Under the assumption of a uniform contribution over each interval this becomes simply the average value. Alternatively one can use again the information of the contribution of subsequent profiles in order to calculate the mean value. Figure 32 shows the results obtained for a $50\,\mu m$ interval size and usage of the average value. Figure 33 shows the quality of the reconstruction in dependency of the interval size. This method yields very regular oscillations whose extent is generally smaller than that for the other methods which use a weighted point spread function on the whole interval. Also the results show basically no difference between the usage of the average value and the arithmetic mean which can be ascribed to the fact that the contribution of partial profiles changes smoothly on every interval (compare Fig. 23) and thus the arithmetic mean is similar to the average value.

6.3.2. Performance for non-uniform transmission

In this section the effect of the artificially introduced, non-uniform transmission through the sieve on the quality of the reconstruction is investigated. For this purpose the simulation data has been additionally modified in such a way that it corresponds to the transmission described by equation (24).

Weighted point spread functions

The underlying actual contributions of different gyroradii are assumed to be constant on

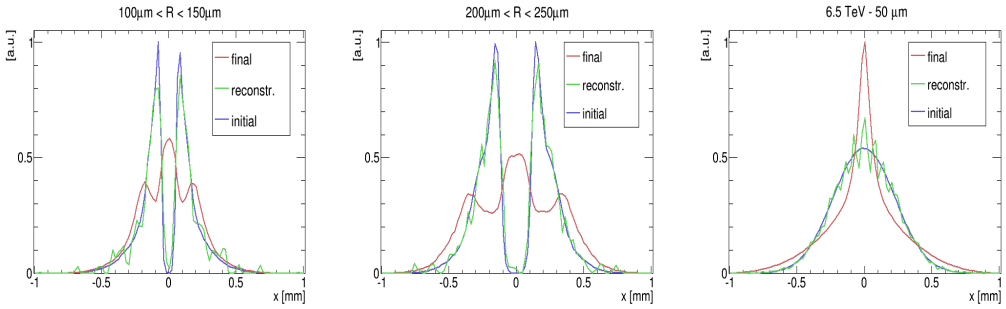

Figure 32: Reconstruction of the beam profile for a binning of 50 μm. A single point spread function corresponding to the average gyroradius of each interval was used.

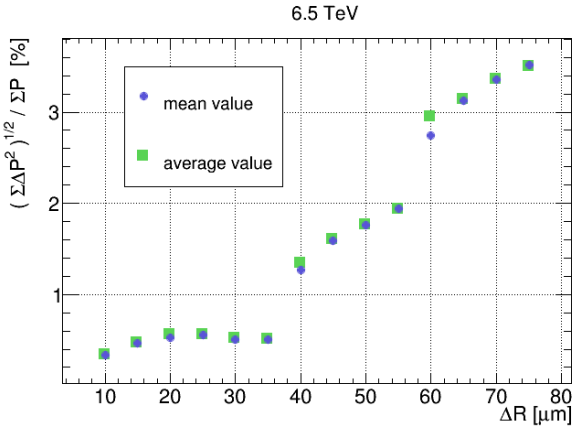

Figure 33: Deviation of the reconstructed profile from the original beam profile for different binnings of the sieve. A single point spread function corresponding to the mean and average value of each interval was used.

each interval and thus only the contributions emerging from the non-uniform transmission have been considered in order to obtain the weights for the intrinsic point spread functions after equation (33). Figure 34 shows the quality of the reconstruction in dependency of the used interval size. While the quality of the results is good for small interval sizes it is obviously decreasing for larger interval sizes which can be ascribed to the fact that the assumption of a uniform shape of the intrinsic profiles is not accurate, especially for large interval sizes (compare Fig. 24). Compared to the case of uniform transmission (see Fig. 31) the quality of the results is less because the resulting partial profiles actually contain electrons on intervals double as large as for uniform transmission, according to equation (24) and thus the error in deconvolution increases accordingly.

Single point spread functions

As an alternative a single point spread function was used (as already in the case of uniform transmission), corresponding to the mean value of transmission for each interval (that is R_i if one neglects the underlying contributions, compare equation (24)). Figure 35 shows the quality of the reconstruction in dependency of the used interval size. The plot shows very

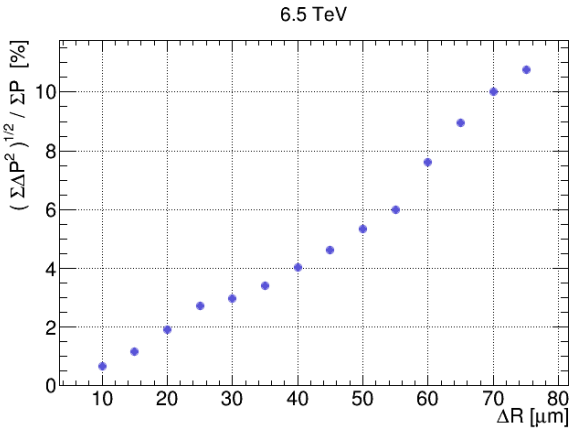

Figure 34: Deviation of the reconstructed profile from the original beam profile for different binnings of the sieve. The non-uniform transmission introduced by the sieve was considered. A weighted point spread function with weights obtained after equation (33) was used.

good results for small interval sizes while the quality of the results is decreasing steadily for larger intervals.

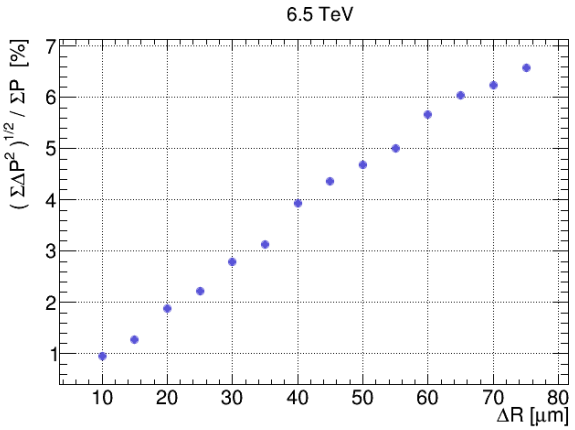

Figure 35: Deviation of the reconstructed profile from the original beam profile for different binnings of the sieve. The non-uniform transmission introduced by the sieve was considered. A single point spread function corresponding to the mean gyroradius of each interval was used.

The quality of the results is less compared to the case of uniform transmission (see Fig. 33) because the resulting partial profiles actually contain electrons on intervals that are double as large as for uniform transmission, according to equation (24) and thus the error in deconvolution increases accordingly.

Amongst the different tested point spread functions the concept of a single point spread function corresponding to the mean gyroradius of the respective interval turned out to yield the best results.

6.4. Further considerations

6.4.1. Material for the sieve

When considering the actual implementation of an electron sieve the question arises which material should be used for its construction. The material must meet specific requirements:

- *conductivity*; as the sieve is supposed to absorb electrons it must be grounded in order to discharge continuously.
- *no secondary electron emission*; secondary electrons - if recorded - introduce noise into the detector profile; primary electrons have velocities of around 9% of the velocity of light when they reach the detector; however secondary electrons will have much smaller energies when they reach the MCP and thus will likely not trigger a signal.
- *radiation hardness*; as all equipment in the LHC tunnel it must not change its properties under the influence of radiation.
- *vacuum compatibility*; because of the very low gas pressure in the ionization chamber the material must have a low outgassing.

The plate for the electron sieve could be made of lead glass or graphite for example. Both materials have a low secondary electron yield and also meet the other requirements.

6.4.2. Effect of noise on the reconstruction

In section 6.1 the acquisition of the different partial profiles with an electron sieve was discussed. Because of the non-uniform transmission with respect to the gyroradius of electrons a way of profile subtraction has been introduced in order to obtain profiles which correspond to the required intervals. Equation (23) describes how to calculate those partial profiles in a recursive manner from the different registered profiles. All investigations were done for an ideal case without any influence of noise. However for a real measurement the obtained signal will be accompanied by noise

$$P_{[0,R_i]} \rightarrow P_{[0,R_i]} + H_i \tag{36}$$

where H_i is the noise recorded by gap i. Noise may vary with the position along x and z as well as in time and will depend on the setup of the detector and its environment. If the contribution of noise $H(x, z, t)$ is precisely known it can be cancelled from the registered profiles before calculating the partial profiles from them. If noise is not sufficiently removed from the profiles its remainder will be amplified by the recursive subtraction of profiles and accordingly affect the quality of the results of the deconvolution method. The extent to which noise affects the reconstruction of the beam profile remains to be investigated as well as a study of noise in the installed devices needs to be done.

6.4.3. Electron interference at the sieve

It is important that the electrons do not show any interference due to diffraction at the gaps of the sieve as this would lead to a signal at different positions. The de-Broglie wavelength

of an electron with velocity $v \approx 0.09c$ is:

$$\lambda = \frac{h}{p} \quad \Rightarrow \quad \lambda_e \approx 2.69 \cdot 10^{-11}\, m \ll 1\,\mu m \tag{37}$$

The wavelength of electrons is much smaller than the size of the gaps and therefore no diffraction will be visible.

7. Conclusions

At first different models for the description of the ionization process were compared with each other in order to find an optimal way of generating the initial momenta of electrons because this aspect is not covered directly by the simulation code. As the approach of energy loss of incident particles in a material, implemented in Geant4, turned out to yield wrong results, different double differential cross sections covering the relativistic speeds of the incident particles were presented. The cross section presented by Voitkiv was preferred to the Bethe approach because the crucial part for slow emitted electrons is considered to yield more reliable values. The corresponding initial gyroradius distribution contains mostly small gyroradii ($< 40\,\mu m$) compared to the used binning ($10\,\mu m$ for the simulation, $110\,\mu m$ for the camera which is actually used for recording the signal).

As the increase of gyroradii is minor at the tails of the emerging electron distribution (the increase follows approximately the bunch electric field) the profile distortion is visible in the center, which results in strongly non-Gaussian shapes. Both the bunch electric field and the profile distortion depend strongly on the transverse beam size. On the one hand a stronger bunch electric field causes a greater enlargement of gyroradii while on the other hand the beam size decreases compared to the emerging gyroradii making any distortions more visible.

A mechanism of profile distortion was established considering the purely circular movement of the electrons in the x-z-plane at detector level (after they left the space charge region their movement takes place almost without the influence of the bunch electric field). A probability based model for the displacement on adjacent bins was established leading to the use of point spread functions which depend on the gyroradii of electrons. This allows for the description of profile distortion via convolution. Requirements such as the following were verified: first the gyration center at detector level deviates only to a minor extent from the production point of an electron and second the concept of a probability is actually justified - provided that the movement of electrons towards the detector does not favor any bins.

This model for describing the profile distortion via convolution and the corresponding reconstruction of the original profile by applying a deconvolution algorithm requires the availability of partial detector profiles each of which contains only electrons of gyroradii within a certain interval because the corresponding point spread functions depend on the gyroradii of electrons again. For the purpose of filtering the electron signal with respect to the gyroradius the concept of an electron sieve was introduced in the form of a plate with rectangular gaps of different widths. The problem of non-uniform transmission of electrons through the sieve with respect to their gyroradii, which emerges from a uniform distribution of gyroradii along the beam and corresponding difficulties of obtaining the required partial profiles were investigated. A method of recursively subtracting the registered profiles from each other was presented, allowing for a confinement of the obtained signals on intervals that correspond to the required ranges of gyroradii. In addition, the resulting transmissions of subsequent partial profiles are complementary so that summing up the partial corrections results in a uniform contribution of electrons of all gyroradii in the totally reconstructed profile. That means that the result will not show any deviations from its Gaussian shape due to the non-uniform transmission of the sieve.

The binning of gyroradii - resulting from the use of a sieve - limits the quality of this method, which goes hand in hand with the quality of the description of the distortion via convolution. The size of the emerging intervals is significant for the quality of the reconstructions because the description of the distortion of a collection of electrons of various gyroradii with one point spread function results in errors in the form of cross terms in the convolution. That means that parts of the collective profile are also convoluted with point spread functions which correspond to different gyroradii. As the shapes of the intrinsic profiles of each group are unknown, a simple adjustment of the profile which is used for the deconvolution is not possible. Different ways of minimizing this error in the deconvolution were discussed, indicating that the use of a single point spread function which corresponds to the mean gyroradius of the respective interval yields the best results. The results of the deconvolution show mostly periodic oscillations around the original profiles, whose extent depends on the binning of the sieve. Reasonable results could be obtained for an interval size of $50\,\mu m$ while the results for interval sizes below $30\,\mu m$ showed a very close agreement with the original profiles.

The investigations were performed for an ideal case without noise, whereas noise, if not known precisely, is expected to have negative effects on this method in the form of an amplification during the calculation of the partial profiles. Especially for high gyroradii the main signal contributes only little to the total obtained signal and thus the cancellation of the mainly contributing, secondary signal can cause large errors if it is not performed precisely. Some requirements for the material of the sieve were mentioned, however, further investigations on this topic remain still to be done.

Appendices

A. Parameter scan for the effective charge of Neon

In order to obtain a meaningful value for the effective charge of Neon, which is required by the model of ionization after Voitkiv et al. [16], a parameter scan was performed where the simulation results are compared against an actual profile measured by one of the IPMs in the LHC for accordingly fixed beam parameters while the normalized emittance and the effective charge are varied. Figure 36 shows the result of this parameter scan. It does not indicate an obvious global minimum for Z_t. However the quality of the IPM data which was used is not very reliable as it contains a lot of noise and therefore the scan might not yield correct results. For this reason the results of the parameter scan are considered to be ineffectual and the theoretical value $Z_t = 5.758$ presented in [4] has been used throughout the investigations which have been performed for this paper.

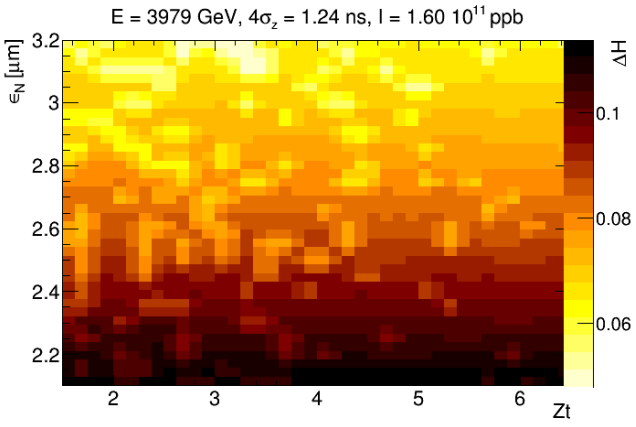

Figure 36: Results of the parameter scan for the effective charge Z_t of Neon. A profile obtained by the vertical device of beam 2 at $E = 3979\,\mathrm{GeV}$, $4\sigma_z = 1.24\,\mathrm{ns}$, $I = 1.60{\cdot}10^{11}$ ppb was compared against the simulation results. $\Delta H \equiv \left(\sum \Delta x_i^2\right)^{-1/2} / \sum x_i$ gives the relative deviation of the simulated profile from the reference profile. The binning is 0.2 and $0.05\,\mu m$ for Z_t and ϵ_N respectively.

B. Proof of equation 24

This proof covers the case of a regular sieve (as defined by equation (22)). Recalling equation (24) we introduce the following shorthands for the different parts of the transmission function:

$$T_{[R_i,R_{i+1}]} = \begin{cases} 0 & ,0 \leq R < R_{i-1} \\ T^1_{[R_i,R_{i+1}]} := R - R_{i-1} & ,R_{i-1} \leq R < R_i \\ T^2_{[R_i,R_{i+1}]} := -R + R_{i+1} & ,R_i \leq R < R_{i+1} \end{cases} \tag{38}$$

The proof is done via mathematical induction. For $i = 0$ the transmission function results as

$$T_{[R_0,R_1]} = \begin{cases} -R + R_1 & ,0 \leq R < R_1 \\ 0 & ,R_1 \leq R \end{cases} \tag{39}$$

and thus the relation is fulfilled. For $i = 1$ the transmission function results as:

$$\begin{aligned} T_{[R_1,R_2]} &= T_{[0,R_2]} - \frac{T_{[0,R_2]}(R_0)}{T_{[0,R_1]}(0)} T_{[0,R_1]} = -R + R_2 - \frac{R_2}{R_1} T_{[0,R_1]} \\ &= -R + R_2 - 2T_{[0,R_1]} \end{aligned} \tag{40}$$

Because $T_{[0,R_1]}$ is only non-zero on the interval $[0, R_1]$ this splits into:

$$T_{[R_1,R_2]} = \begin{cases} R & ,0 \leq R < R_1 \\ -R + R_2 & ,R_1 \leq R < R_2 \\ 0 & ,R_2 \leq R \end{cases} \tag{41}$$

Therefore the relation is also fulfilled for $i = 1$.

The inductive step is:

$$\begin{aligned} T_{[R_{i+1},R_{i+2}]} &= T_{[R_0,R_{i+2}]} - \sum_{j=0}^{i} \frac{T_{[0,R_i+2]}(R_j)}{T_{[R_j,R_{j+1}]}(R_j)} T_{[R_j,R_{j+1}]} \\ &= -R + R_{i+2} + (R_{i+1} - R_{i+1}) \\ &\quad - \sum_{j=0}^{i-1} \frac{-R_j + R_{i+2} + (R_{i+1} - R_{i+1})}{T_{[R_j,R_{j+1}]}(R_j)} T_{[R_j,R_{j+1}]} - \frac{R_{i+2} - R_i}{R_{i+1} - R_i} T_{[R_i,R_{i+1}]} \\ &= T_{[0,R_{i+1}]} - \sum_{j=0}^{i-1} \frac{T_{[0,R_i+1]}(R_j)}{T_{[R_j,R_{j+1}]}(R_j)} T_{[R_j,R_{j+1}]} \\ &\quad - \sum_{j=0}^{i-1} \frac{\Delta R}{T_{[R_j,R_{j+1}]}(R_j)} T_{[R_j,R_{j+1}]} + \Delta R - 2T_{[R_i,R_{i+1}]} \end{aligned} \tag{42}$$

Note that by making the substitution $T_{[0,R_{i+2}]} = T_{[0,R_{i+1}]} + \Delta R$ we change the interval on which the function is defined from $[0, R_{i+2}]$ to $[0, R_{i+1}]$. Therefore this representation holds only on the interval $[0, R_{i+1}]$ and we have to consider the case $R \in [R_{i+1}, R_{i+2}]$ separately.

The first two terms in this expression sum up to $T_{[R_i,R_{i+1}]}$. Also $T_{[R_j,R_{j+1}]}(R_j) = \Delta R$ simplifies the remaining sum. Therefore equation (42) becomes:

$$T_{[R_{i+1},R_{i+2}]} = -T_{[R_i,R_{i+1}]} - \sum_{j=0}^{i-1} T_{[R_j,R_{j+1}]} + \Delta R \tag{43}$$

Consider the 4 different cases:

a) $R_0 \leq R < R_{i-1}$

b) $R_{i-1} \leq R < R_i$

c) $R_i \leq R < R_{i+1}$

d) $R_{i+1} \leq R < R_{i+2}$

Case a)

$T_{[R_i,R_{i+1}]} \equiv 0$. We rewrite the sum using the shorthands defined in equation (38). Note that the different terms in the sum are defined on different intervals while $T^1_{[R_j,R_{j+1}]}$ is defined on the same interval as $T^2_{[R_{j-1},R_j]}$:

$$\begin{aligned}
\sum_{j=0}^{i-1} T_{[R_j,R_{j+1}]} &= T^2_{[R_0,R_1]} + \sum_{j=1}^{i-2} \left(T^1_{[R_j,R_{j+1}]} + T^2_{[R_j,R_{j+1}]} \right) + T^1_{[R_{i-1},R_i]} \\
&= T^2_{[R_0,R_1]} + \sum_{j=1}^{i-2} T^1_{[R_j,R_{j+1}]} + \sum_{j=1}^{i-2} T^2_{[R_j,R_{j+1}]} + T^1_{[R_{i-1},R_i]} \\
&= T^2_{[R_0,R_1]} + T^1_{[R_1,R_2]} + \sum_{j=2}^{i-2} T^1_{[R_j,R_{j+1}]} + \sum_{j=2}^{i-2} T^2_{[R_{j-1},R_j]} \\
&+ T^2_{[R_{i-2},R_{i-1}]} + T^1_{[R_{i-1},R_i]} \\
&= [\Delta R]_{[R_0,R_1]} + \sum_{j=2}^{i-2} \left(T^2_{[R_{j-1},R_j]} + T^1_{[R_j,R_{j+1}]} \right) + [\Delta R]_{[R_{i-2},R_{i-1}]} \\
&= [\Delta R]_{[R_0,R_{i-1}]}
\end{aligned} \tag{44}$$

Thus we obtain:

$$T_{[R_{i+1},R_{i+2}]} = -\Delta R + \Delta R = 0 \quad \square \tag{45}$$

Case b)

$T_{[R_i,R_{i+1}]} \equiv R - R_{i-1}$. Only the last term of the sum is contributing, all others are zero.

$$\begin{aligned}
T_{[R_{i+1},R_{i+2}]} &= -(R - R_{i-1}) - T^2_{[R_{i-1},R_i]} + \Delta R = \\
&= -(R - R_{i-1}) - (-R + R_i) + \Delta R = 0 \quad \square
\end{aligned} \tag{46}$$

Case c)

$T_{[R_i,R_{i+1}]} \equiv -R + R_{i+1}$. Every term of the sum is zero and therefore we obtain:

$$T_{[R_{i+1},R_{i+2}]} = R - R_{i+1} + \Delta R = R - R_i \quad \square \tag{47}$$

Case d)

In this case we cannot make the substitution $T_{[R_0,R_{i+2}]} = T_{[R_0,R_{i+1}]} + \Delta R$ as it changes the interval on which the function is defined. However in this case the original sum in equation (42) (going from 0 to i) is not contributing and therefore the function is simply the transmission function of the last gap:

$$T_{[R_{i+1},R_{i+2}]} = -R + R_{i+2} \quad \square \tag{48}$$

C. Different sieve geometries

In section 6.1 we considered a sieve which consists of rectangular gaps of different widths in order to acquire the different partial profiles (compare Fig. 18). The purpose of the sieve openings is to filter the electron signal with respect to their gyroradii. The sieve openings should cause a transmission that allows to cancel out the secondary, low gyration signal in order to obtain profiles which correspond to the required intervals. The resulting intervals to which the electron gyroradii are confined should be as small as possible. In addition the resulting transmission (after cancellation of the secondary part) should be such that the sum of all partial corrections reflects a uniform transmission for all gyroradii in order to prevent a deviation from the actual Gaussian shape of the overall reconstructed profile. Thus an ideal case would be to have a uniform transmission for all gyroradii which makes the calculation of the partial profiles straight forward by subtraction of two subsequent ones and prevents any non-Gaussianity in the reconstructed profile. When regarding actual measurements one also has to deal with uncertainties and noise in the signal. Therefore a high contribution of the important primary part of the signal to the total signal is favorable. The primary part of the signal is the part which corresponds to the required interval for the respective partial profile. Therefore a high primary signal to signal ratio is preferred. In this section different geometries for the sieve openings are considered in order to find an optimal configuration.

A rectangular gap only confines the electron positions with respect to z, along x the structure is not limited (within the relevant range) and does not change its shape. However if the structure of the sieve openings also confines the positions of electrons with respect to x then the acquisition of partial profiles must be performed by groups of rows where every row is slightly shifted against the previous one (with respect to x) in order to ensure that for every position along x all parts of a sieve opening appear along z. After integration along z each position along x contains electrons which were located above every part of a sieve opening and therefore no alteration of the profile occurs along x (for example for circular sieve openings).

In order to obtain the corresponding transmission in dependency of the gyroradius one needs to consider the area on which the gyration centers of electrons can be located without causing contact to the sieve (in the following called *maximum free area*). The length along z on which the gyration center can be located (in the following called *maximum free length*, denoted with $z_{\max}$) changes along x and thus the maximum free area is given by the integral of $z_{\max}$ along x. In order to compare the different geometries between each other their transmission (that is the maximum free area) will be normalized to the total area that a rectangular gap, which acquires electrons on the same interval of gyroradii, would cover (that is the maximum free area for a rectangular gap for $R = 0$). In order to show the difference in recorded signal between the different geometries the ratio of the transmission of each geometry to the transmission of a rectangular gap is calculated (in the following called *signal ratio*).

C.1. Circular sieve openings

The limitation in gyroradius is directly given by the radius of the circles. As mentioned above the acquisition of the partial profiles must be performed by groups of rows as shown in Fig. 37.

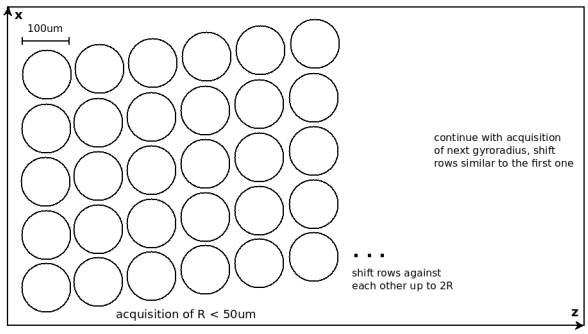

Figure 37: Sketch for a sieve with circular openings. Each partial profile is acquired by a group of rows where each row is slightly shifted against the previous one to ensure a uniform transmission along x.

The transmission for one row within a group is given by $z_{\max}$ at the respective x. Figure 38 visualizes the relevant relations for $z_{\max}$.

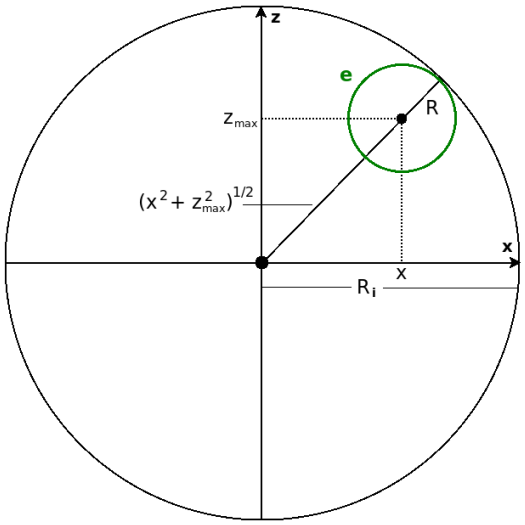

Figure 38: Visualization of the maximum free length $z_{\max}$ at a given position x for circular sieve openings.

Figure 38 shows that for $z_{\max}$ the connection line between the gyration center and the touching point to the sieve also includes the center of the sieve opening. This is because the shortest connection from a point within a circle to its boundary is the perpendicular line on a tangent to circle that includes the point itself. Because every perpendicular line on a tangent to a circle also goes through the center of the circle the three points are aligned. Thus $z_{\max}$ is given by:

$$\sqrt{x^2 + z_{\max}^2} + R = R_i \quad \Rightarrow \quad z_{\max} = \sqrt{(R_i - R)^2 - x^2} \tag{49}$$

Figure 39 shows the dependency of $z_{\max}$ on x for different gyroradii in combination with the circular sieve opening.

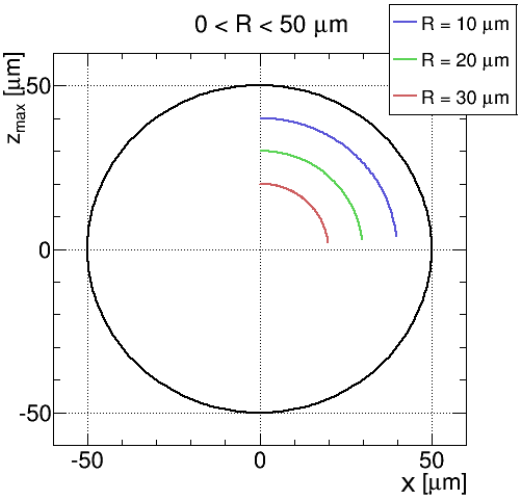

Figure 39: $z_{\max}$ in dependency of x for different gyroradii for circular sieve openings.

The transmission for a group is given by the integral of $z_{\max}$ along x (writing $R_- \equiv R_i - R$):

$$\begin{aligned} T_{[0,R_i]}(R) &= \frac{1}{4R_i^2} \cdot 4 \int_0^{R_-} \sqrt{R_-^2 - x^2}\, dx \\ &= \frac{1}{2R_i^2} \left[x\sqrt{R_-^2 - x^2} + R_-^2 \cdot \arctan\left(\frac{x}{\sqrt{R_-^2 - x^2}} \right) \right]_{x=0}^{x=R_-} \\ &= \frac{\pi}{4} \left(1 - \frac{R}{R_i} \right)^2 \end{aligned} \tag{50}$$

The transmission is normalized to the area covered by a rectangular gap. The integral in equation (50) represents one quadrant and is thus multiplied by four. The signal ratio to an equivalent rectangular gap is given by:

$$\frac{T_C}{T_R} = \frac{\pi}{4} \left(1 - \frac{R}{R_i} \right) \tag{51}$$

Figure 40 shows the transmission for circular sieve openings together with the one for rectangular gaps (compare Fig. 20). The transmission for circular sieve openings has a quadratic dependency on the gyroradius with a minimum at R_i. This means that one obtains less signal in the important interval $[R_i, R_{i+1}]$. In addition it is more difficult to cancel out the secondary, low gyration part of the signal which is necessary in order to obtain a good quality for the results of the deconvolution procedure.

The ratio of the primary signal ($[R_i, R_{i+1}]$) to the total signal ($[0, R_{i+1}]$) recorded by the corresponding group is:

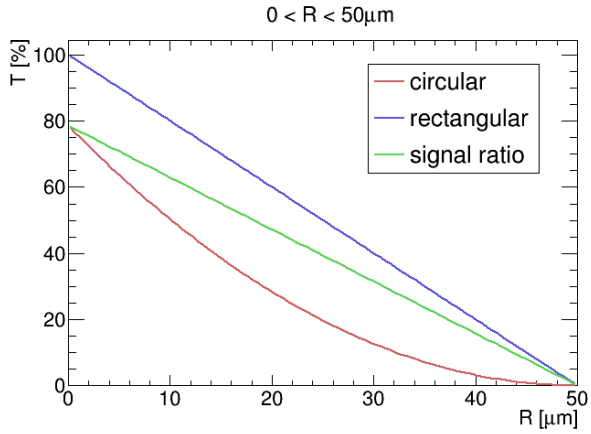

Figure 40: Transmission for circular sieve openings compared against the transmission for rectangular openings.

$$\left[1 - \frac{R_i}{R_{i+1}}\right]^3 \tag{52}$$

Thus the contribution of the primary signal will decrease strongly for the acquisition of larger gyroradii.

C.2. Triangular sieve openings

In this case the gyroradii of electrons are confined by the radius of the incircle of each triangle. Although triangles can be aligned such that they are complementary to a rectangle the acquisition cannot be performed by a single row because the transmission will only be uniform for $R = 0$. For $R > 0$ the position of the gyration center is limited with respect to x and therefore some parts of the triangle do not have a complement. Within this non-complementary range the transmission depends on x and therefore cause a change in the profile. Figure 41 shows a sketch for a sieve with triangular openings.

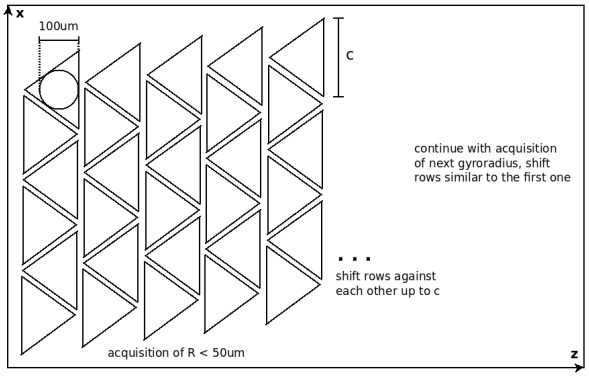

Figure 41: Sketch for a sieve with triangular openings. Each partial profile is acquired by a group of rows where each row is slightly shifted against the previous one to ensure a uniform transmission along x.

Figure 42 shows the relations for the maximum free length $z_{\max}$ within a triangle. It is given by

$$z_{\max} = h(x) - p - R \tag{53}$$

where $h(x)$ and p are given by:

$$h(x) = \left(\frac{c}{2} - x\right) \cdot \tan\alpha \qquad , \qquad p = \frac{R}{\cos\alpha} \tag{54}$$

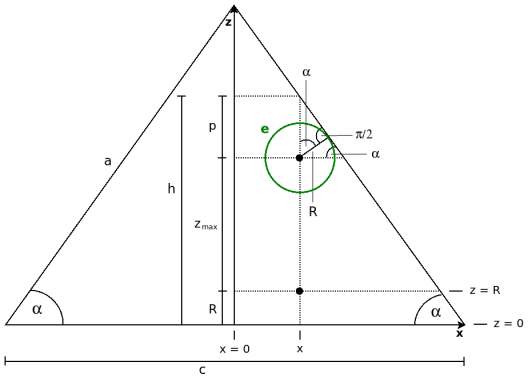

Figure 42: Visualization of the maximum free length $z_{\max}$ at a given position x for triangular sieve openings.

The position of the gyration center is limited with respect to x for $R \in [0, R_i]$ as follows

$$z_{\max} \stackrel{!}{=} 0 \qquad \Rightarrow \qquad x_{\max} = \frac{c\sin\alpha - 2R(1+\cos\alpha)}{2\sin\alpha} =: \frac{q(R)}{\sin\alpha} \tag{55}$$

with

$$q(R) = \frac{c\sin\alpha - 2R(1+\cos\alpha)}{2}$$

Using the expression $q(R)$ we can rewrite $z_{\max}$:

$$z_{\max} = \frac{q(R)}{\cos\alpha} - x\tan\alpha \tag{56}$$

Figure 43 shows the dependency of $z_{\max}$ on the position along x for different gyroradii in combination with the triangular sieve opening and its incircle.

The incircle radius R_i of a triangle is given by (for the sake of readability the subscript i has been spared for c and α; however in order to obtain a signal on a different interval one has to change c_i and/or α_i accordingly):

$$R_i = \frac{c^2\tan\alpha}{2} \cdot \frac{1}{\frac{c}{\cos\alpha} + c} = \frac{c}{2} \cdot \frac{\sin\alpha}{1+\cos\alpha} \tag{57}$$

This relation also defines the shape of a triangle in order to obtain a signal on the interval $[0, R_i]$. Accordingly we can rewrite $q(R)$ by replacing c with R_i:

$$q(R) = (1+\cos\alpha)(R_i - R)$$

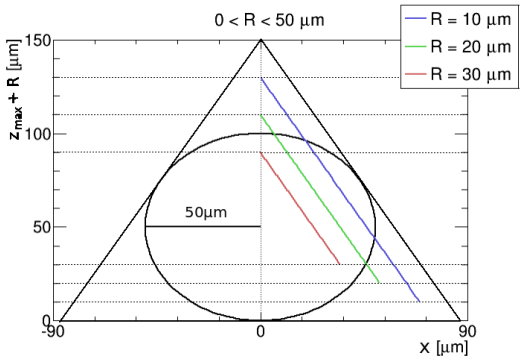

Figure 43: $z_{\max}$ in dependency of x for different gyroradii for equilateral triangular sieve openings.

Because the triangles are aligned in an alternating way (compare Fig. 41) the actual maximum free length is the sum of the maximum free lengths of the two complementary triangles. One has to distinguish two cases:

a) $\frac{c}{4} < x_{\max} < \frac{c}{2} \quad \Leftrightarrow \quad 0 < R < \frac{R_i}{2}$: some parts have a complement

b) $0 < x_{\max} < \frac{c}{4} \quad \Leftrightarrow \quad \frac{R_i}{2} < R < R_i$: no part has a complement

For case a) the transmission is calculated as follows (normalized to the area of a rectangular gap; writing $c_2 \equiv \frac{c}{2}$):

$$\begin{aligned} T^{a)}_{[0,R_i]}(R) &= \frac{1}{\frac{c}{2}\cdot 2R_i}\int_0^{c_2}\left[z_{\max}(x)+z_{\max}(c_2-x)\right]\,dx \\ &= \frac{1}{c\cdot R_i}\left[\int_0^{c_2-x_{\max}} z_{\max}(x)\,dx + \int_{c_2-x_{\max}}^{x_{\max}}\left[z_{\max}(x)+z_{\max}(c_2-x)\right]\,dx\right. \\ &\left. + \int_{x_{\max}}^{c_2} z_{\max}(c_2-x)\,dx\right] \\ &= \frac{\sin\alpha}{2R_i^2(1+\cos\alpha)}\cdot\frac{q(R)^2}{\sin\alpha\cos\alpha} \\ &= \frac{1+\cos\alpha}{2\cos\alpha}\cdot\left(1-\frac{R}{R_i}\right)^2 \end{aligned} \tag{58}$$

For case b) the transmission is calculated as (again normalized to the area of a rectangular gap; with $c_2 \equiv \frac{c}{2}$):

$$
\begin{aligned}
T^{b)}_{[0,R_i]}(R) &= \frac{1}{cR_i}\left[\int_0^{x_{\max}} z_{\max}(x)\,dx + \int_{c_2-x_{\max}}^{c_2} z_{\max}(c_2-x)\,dx\right] \\
&= \frac{\sin\alpha}{2R_i^2(1+\cos\alpha)} \cdot \frac{2q(R)^2}{\sin\alpha\cos\alpha} \\
&= \frac{1+\cos\alpha}{2\cos\alpha}\left(1-\frac{R}{R_i}\right)^2
\end{aligned}
\tag{59}
$$

Both cases have the same dependency on the gyroradius. Thus the signal ratio to an equivalent rectangular gap is:

$$
\frac{T_T}{T_R} = \frac{1+\cos\alpha}{2\cos\alpha}\left(1-\frac{R}{R_i}\right) \tag{60}
$$

Figure 44 shows the transmission for equilateral triangles together with the transmission of a corresponding rectangular gap. As for circular sieve openings the transmission has a quadratic dependency on the gyroradius which implies a signal decrease on the essential interval as well as difficulties to cancel out the secondary, low gyration part of the signal.

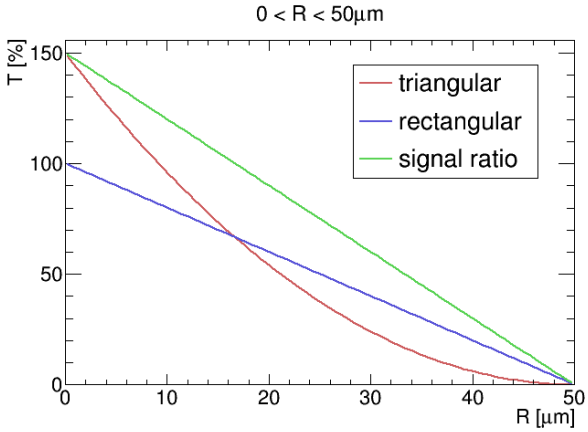

Figure 44: Transmission for equilateral triangular sieve openings compared against the transmission for rectangular openings.

The ratio of the primary signal ($[R_i, R_{i+1}]$) to the total signal ($[0, R_{i+1}]$) recorded by the corresponding group is:

$$
\left[1-\frac{R_i}{R_{i+1}}\right]^3 \tag{61}
$$

As for circular sieve openings the contribution of the primary signal will decrease strongly for the acquisition of larger gyroradii.

C.3. Concentric circles

The idea is to combine a circular sieve opening (of radius R_2) with a smaller circular, non-transmissive element (of radius R_1) in its center in order to allow only electrons above a

certain gyroradius to pass. The acquisition is performed similar to circular sieve openings (group-wise, row-wise shifted) as shown in Fig. 37.

This combination of two circles will allow low gyration electrons to pass on the one hand (between the two circles, see Fig. 45, left), as well as electrons with gyroradii above the radius of the inner circle on the other hand (see Fig. 45, right) which correspond to the essential interval.

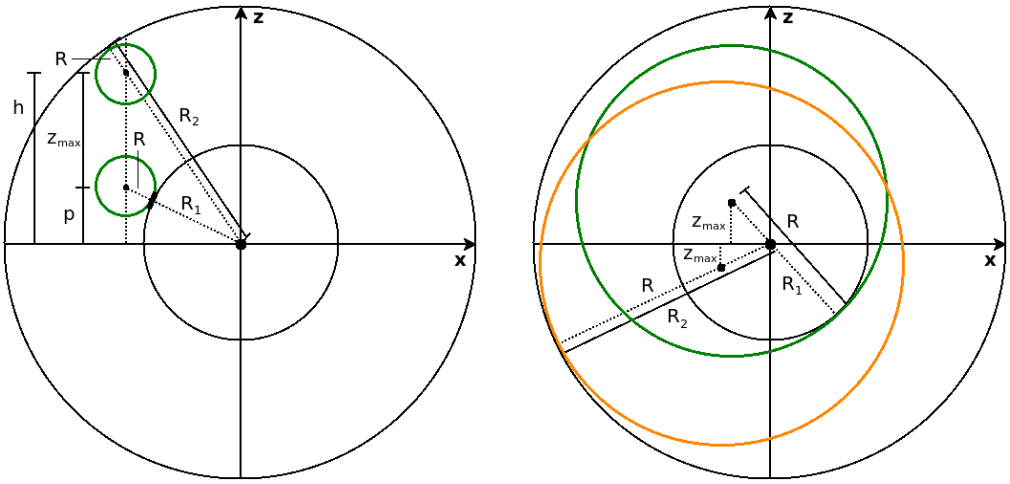

Figure 45: Visualization of the maximum free length $z_{\max}$ at given positions x for a concentric circle geometry.

We have to consider four different cases for the calculation of the transmission (we will consider the right upper quadrant for the calculations):

1. $0 \leq R < \frac{R_2 - R_1}{2}$
   a) $0 \leq x < (R_1 + R)$
   b) $(R_1 + R) < x < (R_2 - R)$
2. $R_1 < R < R_2$
   a) $R_1 < R < \frac{R_1 + R_2}{2}$
   b) $\frac{R_1 + R_2}{2} < R < R_2$

Case 1

For the calculations we will use the following shorthands:

$$R_+ \equiv R_1 + R \qquad R_- \equiv R_2 - R$$
$$R_{12}^+ \equiv \frac{R_1 + R_2}{2} \qquad R_{12}^- \equiv \frac{R_2 - R_1}{2} \tag{62}$$

In case 1.a $z_{\max}$ is bounded below by the inner circle and bounded above by the outer circle (compare Fig. 45, left). In case 1.b $z_{\max}$ has no lower boundary (within the respective

quadrant) and is only bounded above by the outer circle (compare Fig. 38). The same calculations as for the circular sieve openings apply (see section C.1).

1.a) $z_{\max}$ is given by:

$$z_{\max} = h(x) - p(x) = \sqrt{R_-^2 - x^2} - \sqrt{R_+^2 - x^2} \tag{63}$$

1.b) $z_{\max}$ is given by:

$$z_{\max} = \sqrt{R_-^2 - x^2} \tag{64}$$

The transmission is proportional to the area covered by $z_{\max}$ along x:

$$\int_0^{R_-} z_{\max}\, dx = \int_0^{R_+} z_{\max}\, dx + \int_{R_+}^{R_-} z_{\max}\, dx = \frac{\pi}{4} \cdot \left(R_-^2 - R_+^2\right) \tag{65}$$

This represents the maximum free area for one quadrant. The transmission is normalized to the area of a rectangular gap:

$$\begin{aligned} T_{[0,R_2]} &= \frac{\pi}{4} \frac{R_-^2 - R_+^2}{R_2^2} = \frac{\pi}{4} \frac{R_2^2 - R_1^2 - 2R(R_1 + R_2)}{R_2^2} \\ &= \pi \frac{R_{12}^+ R_{12}^- - R R_{12}^+}{R_2^2} \qquad \text{for} \quad 0 \le R < R_{12}^- \end{aligned} \tag{66}$$

Case 2

The purpose of the concentric circles is to constrain the signal to electrons with gyroradii between the radius of the inner and the radius of the outer circle. While the low gyration part described in case 1 is only an undesired by-product, the signal of case 2 is the primary one. For case 2.a $z_{\max}$ is confined by the inner circle and for case 2.b the outer circle is the constraining part.

2.a) $z_{\max}$ is given by:

$$z_{\max} = \sqrt{(R - R_1)^2 - x^2} \tag{67}$$

2.b) $z_{\max}$ is given by:

$$z_{\max} = \sqrt{(R_2 - R)^2 - x^2} \tag{68}$$

Those equations are similar to the one for circular sieve openings (see section C.1) and similarly one obtains the transmission (integration of $z_{\max}$ over x, normalized to the area of a rectangular gap):

$$T_{[0,R_2]} = \begin{cases} \pi \frac{R_{12}^+ R_{12}^- - R R_{12}^+}{R_2^2} & , 0 \le R < R_{12}^- \\ \frac{\pi}{4} \frac{(R-R_1)^2}{R_2^2} & , R_1 < R < R_{12}^+ \\ \frac{\pi}{4} \frac{(R_2-R)^2}{R_2^2} & , R_{12}^+ < R < R_2 \end{cases} \tag{69}$$

The signal ratio to an equivalent rectangular gap is:

$$\frac{T_{NC}}{T_R} = \begin{cases} \frac{\pi R_{12}^+}{R_2} \left(1 - \frac{R_{12}^+}{R_2 - R}\right) & , 0 \le R < R_{12}^- \\ \frac{\pi}{4} \frac{(R-R_1)^2}{R_2(R_2-R)} & , R_1 < R < R_{12}^+ \\ \frac{\pi}{4} \left(1 - \frac{R}{R_2}\right) & , R_{12}^+ < R < R_2 \end{cases} \tag{70}$$

Figure 46 shows the transmission for concentric circles together with the one for a rectangular gap.

The secondary signal is linear in R and corresponds to a constant interval if $R_2 - R_1$ is kept constant over all groups. A similar signal can be obtained by a rectangular gap of width $R_2 - R_1$ which differs only by a scaling factor from this secondary signal (compare section 6.1.1). Thus if the acquisition is performed by groups of concentric circles with constant $R_2 - R_1$ an additional gap of that width can be installed in order to identify the secondary signal from low gyration electrons and cancel it from the registered profiles.

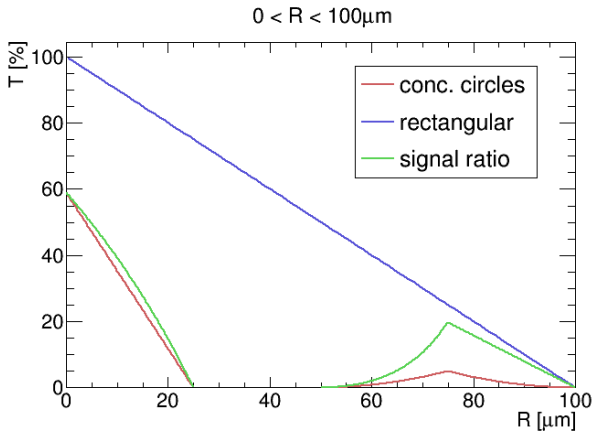

Figure 46: Transmission for concentric circles compared against the transmission for rectangular sieve openings.

The ratio of the primary signal ($[R_i, R_{i+1}]$) to the total signal ($[0, R_{i+1}]$) recorded by the corresponding group is:

$$\frac{1 - \frac{R_i}{R_{i+1}}}{4 + 2\frac{R_i}{R_{i+1}}} \tag{71}$$

Thus the contribution of the primary signal to the total signal will decrease less strongly for $R_i/R_{i+1} >\approx 3/4$ than for circular and triangular sieve openings.

C.4. Comparison

Figure 47 shows a comparison of the transmissions for the different geometries. Circular and triangular sieve openings show a quadratic dependency on the gyroradius with a signal on the whole range $[0, R_i]$, in contrast to rectangular gaps that have a linear dependency on the gyroradius. In all three cases the ratio of the main signal on $[R_i, R_{i+1}]$ to the total signal on $[0, R_{i+1}]$ is of the form

$$\left[1 - \frac{R_i}{R_{i+1}}\right]^{\gamma} \tag{72}$$

where $\gamma = 3$ for circular and triangular sieve openings and $\gamma = 2$ for rectangular gaps. This does not account for the actual underlying electron gyroradius distribution but only for the transmission of different gyroradii.

The ratio of the primary signal to the total signal decreases faster for circular and triangular sieve openings than for rectangular gaps. It is also more difficult to cancel the secondary signal for a quadratic dependency than for a linear dependency (as it happens to be for rectangular gaps).

The ratio of the main signal to the total signal for concentric circles is

$$\frac{1 - \frac{R_i}{R_{i+1}}}{4 + 2\frac{R_i}{R_{i+1}}} \tag{73}$$

and thus decreases less fast than for the other three geometries for intervals above $R_i/R_{i+1} >\approx 3/4$.

The strength of the primary signal one obtains for concentric circles is generally lower than for the other geometries. The ratios of the primary signals of the different geometries to the one of a rectangular gap is given by:

$$\frac{MS}{MS_R} = \sigma\left(1 - \frac{R_i}{R_{i+1}}\right) \quad , \quad \text{where} \quad \sigma = \begin{cases} \frac{\pi}{12} & \text{circular} \\ \frac{1}{2} & \text{triangular} \\ \frac{\pi}{48} & \text{concentric circles} \end{cases} \tag{74}$$

The dependency of the primary signal ratio on the gyroradius is the same for all geometries and is decreasing for larger gyroradii. Circular sieve openings have the highest ratio, followed by triangular openings and concentric circles. The strongest primary signal is obtained for rectangular gaps.

However this considers only the artificially introduced non-uniform transmission which occurs on top of the actual underlying gyroradius distribution. The actual properties of the underlying distribution likely change the ratio of primary signal to total signal as described in equation (72) and (73). Figure 48 shows the ratio of primary signal to total signal for the different geometries under consideration of the actual underlying gyroradius distribution (corresponding to the simulation data for the 6.5 TeV case). One can observe that concentric

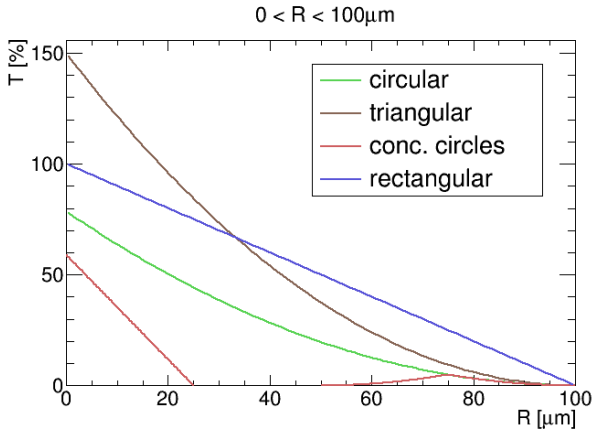

Figure 47: Comparison of the transmission for the different geometries.

circles have the highest ratio for groups with $R_i >\approx 200\,\mu m$. Rectangular gaps have the highest ratio for smaller gyroradii.

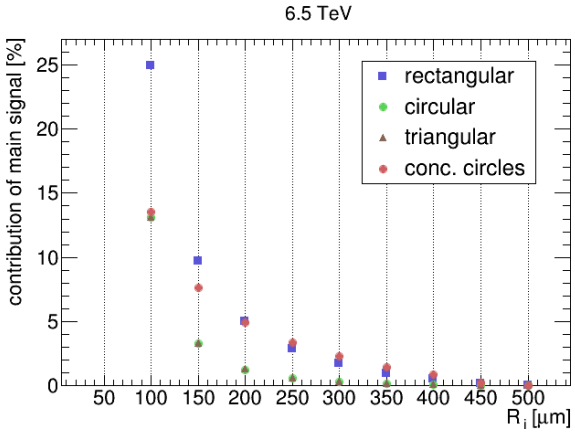

Figure 48: Contribution of the primary signal to the total signal that will be recorded by a group of sieve openings. R_i denotes the upper limit in gyroradius for each sieve opening.

Because of the quadratic dependency of the transmission on the gyroradius for circular and triangular sieve openings it is difficult to cancel the secondary signal from the registered profiles. In addition they show a lower primary signal to signal ratio than the other geometries and their primary signal strength is lower than for rectangular gaps. With concentric circles - in combination with a leading gap of width $R_2 - R_1$ - one is able to obtain a signal on the required gyroradius intervals. The primary signal to signal ratio becomes better than the one for rectangular gaps above a certain limit. However the primary signal strength in general is low compared to rectangular gaps. Also the construction of this geometry is rather complicated (the inner non-transmissive part needs a thin connection to the outer part which must be small enough in order to not affect the spiraling electrons). Therefore a sieve with rectangular gaps is considered to be the most favorable solution. This geometry allows to cancel secondary parts of the registered signals and the emerging transmission of the partial

corrections is complementary in such a way that the overall reconstructed profile will not show any deviation from its Gaussian shape (due to non-uniform transmission). Also the easier feasibility of constructing rectangular gaps features this version.

D. Variations of the electron sieve method

The purpose of this chapter is to present ideas which are related to the separation of electrons with respect to their gyroradii.

D.1. Variation of the magnetic field

Instead of using gaps of different widths one could use gaps of constant width and vary the magnetic field strength over a longer period of time. Because the gyroradii depend on the magnetic field as $R = p(qB)^{-1}$ a decrease of the magnetic field strength will lead to greater gyroradii and therefore the gaps will acquire electrons which corresponded to smaller gyroradii at the maximal magnetic field. All electrons with gyroradii greater than the gap width will not pass. The width of the gap must be chosen such that it covers all gyroradii that occur at the maximal magnetic field $B_{\max}$. A decrease of the magnetic field leads to an increase of gyroradii and while the gyroradius of passing electrons is still confined by the width of the gap those electrons correspond to a different interval at $B_{\max}$. If for example one acquires electrons with gyroradii from 0 to 500 μm at $B_{\max}$ a reduction of the magnetic field strength to half of its value will lead to a doubling of the gyroradii and therefore the gaps will acquire only electrons which had gyroradii between 0 and 250 μm at $B_{\max}$. This is the same interval that a gap of width 250 μm would acquire at $B_{\max}$.

By decreasing the magnetic field stepwise one can "simulate" the acquisition with gaps of different widths. However this method suffers from the problem that although with a smaller magnetic field one can acquire electrons which corresponded to originally smaller gyroradii, those gyroradii are always inflated on an interval of the same width - namely the width that corresponds to the maximal magnetic field strength $B_{\max}$. This is why one cannot resolve the intrinsic parts of each inflated group of gyroradii which is necessary in order to cancel out the secondary, low gyration part of the registered signals. Gaps of different width instead imply different cutoff values for the signal with respect to the gyroradius and the same parts of low gyration are also contained in signals corresponding to higher cutoff values, only to a different extent. However in case of different magnetic field strengths the parts of the signal corresponding to different cutoff values at $B_{\max}$ are altered by an inflation of gyroradii and therefore actually have different shapes in the parts of the signal obtained in the multiple steps. In order to be able to describe the distortion correctly via convolution one needs to confine the contributing gyroradii for each partial profile. For that purpose one needs to remove the low gyration signal from the obtained profiles. The inflation of gyroradii on the same interval makes that unfeasible as the possibility to resolve any contributions is limited to the width of the gaps which actually remains constant.

D.2. Variation of the depth of the sieve

Instead of installing a sieve with gaps of different widths perpendicular to the magnetic field lines one could use a sieve with gaps of constant width but varying thickness and tilt the sieve towards the magnetic field lines. This will lead to different effective gap widths and thus allows for the acquisition of different intervals with respect to the gyroradii of electrons.

The requirement that the widths of the gaps are constant is not necessary but depends on the effective widths one wants to obtain. The benefit of this method would be that one can produce gaps of widths that are actually smaller than it is feasible to construct. Figure 49 shows the sketch of a sieve which is tilted with the angle θ towards the magnetic field lines.

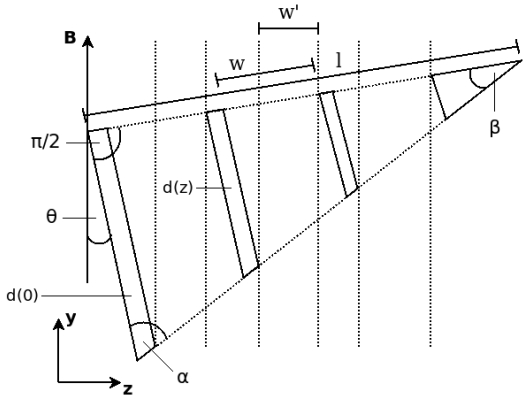

Figure 49: Sketch of a sieve with constant gap width and varying thickness. The sieve is tilted towards the magnetic field lines with the angle θ.

The problem with this concept is that the effective widths of the gaps are not limiting the maximal gyroradius because the effective boundaries limit the movement only in one point each. If an electron performs for example one revolution within the gap and starts at the lower effective boundary it can actually cross over the upper effective boundary because the corresponding limiting point is located on top of the sieve and the actual limit shifts to higher values for z while moving within the gap. The number of revolutions within the gap defines the maximal gyroradius that can pass however it cannot be constrained to the effective width of a gap. Because the different gaps have different thicknesses and thus correspond to different numbers of revolutions the uncertainty in gyroradius changes with each gap.

D.3. Stacked sieves

Instead of using one sieve with gaps of different widths one can stack two sieves in order to let only electrons with specific properties pass at each position. Both sieves consist of small gaps which are shifted against each other in such a way that the distance between them determines the gyroradius which can pass. If the gaps are shifted with respect to z and the distance between the two sieves is chosen such that electrons perform half a revolution in between them then movement in the x-z-plane will span over the full z-range and they will reach the second sieve at the same x-position as they reached the first one which, at the same time, is the x-position of their gyration center and because the electrons spiral basically around their production point (compare Fig. 14) no distortion with respect to x will occur. Figure 50 shows a sketch of two stacked sieves.

The time that an electron needs to move from the first gap to the second one is given by

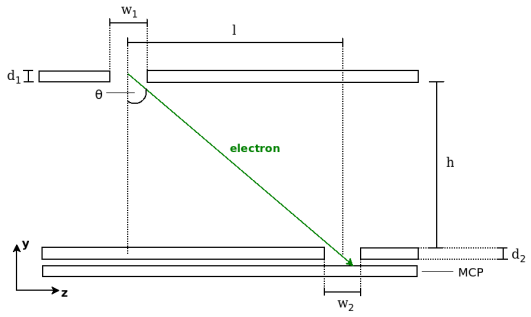

Figure 50: Sketch of two stacked sieves. The trajectory of the electron is indicated to be linear but in fact it is parabolic due to the acceleration by the external extraction field.

$$\begin{aligned} h &= \frac{a}{2} \cdot t^2 + v_y \cdot t \\ t &= \frac{v_y}{a} \left[\sqrt{1 + \frac{2ah}{v_y^2}} - 1 \right] \end{aligned} \tag{75}$$

where $a = \tilde{q}E$ is the acceleration of electrons with the reduced charge $\tilde{q} = qm^{-1}$. In order to prevent distortion with respect to x the electrons are supposed to perform half a revolution between the two plates:

$$\frac{T}{2} = \frac{\pi}{\tilde{q}B} \stackrel{!}{=} t \tag{76}$$

From this requirement one can deduce the required distance of the plates:

$$h = \frac{\pi}{2\tilde{q}} \cdot \frac{\pi E + 2v_y B}{B^2} \tag{77}$$

In order to let electrons of gyroradius R pass the distance between to shifted gaps with respect to z is $l = 2R$.

The requirement that all electrons perform exactly half a revolution between the plates implies that all electrons have the same y-velocity when they reach the first one. However the electrons actually reach the detector with different velocities with respect to y although the variance is rather small for all beam energies as shown in Fig. 19. If the gaps are infinitesimally wide and the plates infinitesimally thin only electrons that arrive at the right position, with the right gyroradius, the right y-velocity and the right phase will be able to pass through the stacked sieve. However in case of a finite width and thickness of the plates electrons of different gyroradii can pass while they can have the reference y-velocity as well as a different one, where the latter causes them to perform not exactly half a revolution in between the plates. The widths of the gaps and the thicknesses of the plates must be chosen in such a way that the passing gyroradii vary as little as possible from the desired values.

References

[1] M. Bassetti, G.A. Erskine: *Closed expression for the electrical field of a two-dimensional gaussian charge*, CERN-ISR-TH-80-06, European Organization for Nuclear Research, Geneva, March 1980

[2] Beam Gas Ionization Monitors, http://bgi.web.cern.ch/

[3] H. Bethe: *Zur Theorie des Durchgangs schneller Korpuskularstrahlen durch Materie*, Annalen der Physik **397**, 325–400, 1930

[4] E. Clementi, D.L. Raimondi, W.P. Reinhardt: *Atomic Screening Constants from SCF Functions*, J.Chem.Phys. **38**, No. 11, 2686–2689, 1963

[5] Jan Egberts: *IFMIF-LIPAc Beam Diagnostics: Profiling and Loss Monitoring Systems*, PhD thesis, Universite Paris - Sud XI, 2012

[6] Geant4: A toolkit for the simulation of the passage of particles through matter, http://geant4.cern.ch/

[7] G. Iadarola: *Electron cloud studies for CERN particle accelerators and simulation code development*, CERN-THESIS-2014-047, European Organization for Nuclear Research, Geneva, 2014

[8] International Commission on Radiation Units and Measurements: *Secondary Electron Spectra from Charged Particle Interactions*, ICRU report **55**, Bethesda, Maryland, 1996

[9] Yong-Ki Kim, M.Eugene Rudd: *Binary-encounter-dipole model for electron-impact ionization*, Physical Review A **50**, No. 5, 3954–3967, 1994

[10] Marcin Patecki: *Analysis of LHC Beam Gas Ionization monitor data and simulation of the electron transport in the detector*, CERN-THESIS-2013-155, European Organization for Nuclear Research, Geneva, 2013

[11] Foster F. Rieke, William Prepejchal: *Ionization Cross Sections of Gaseous Atoms and Molecules for High-Energy Electrons and Positrons*, Physical Review A **6**, No. 4, 1507–1519, 1972

[12] ROOT: A Data Analysis Framework, https://root.cern.ch/
https://root.cern.ch/root/html/TSpectrum.html#TSpectrum:Deconvolution
https://root.cern.ch/root/html/TH1.html#TH1:Fit

[13] M.E. Rudd, Y.-K. Kim, D.H. Madison, T.J. Gay: *Electron production in proton collisions with atoms and molecules: energy distributions*, Reviews of Modern Physics **64**, No. 2, 441–490, 1992

[14] M. Sapinski: *Calibration of LHC BGI monitor with orbital bump*, EDMS 1130606, 2011

[15] D. Vilsmeier, B. Dehning, M. Sapinski: *Investigation of the Effect of Beam Space-Charge on Electron Trajectories in Ionization Profile Monitors*, MOPAB42, Proceedings of HB2014, East Lansing, MI, USA, 2014

[16] Alexander B. Voitkiv, Norbert Gruen, Werner Scheid: *Hydrogen and helium ionization by relativistic projectiles in collisions with small momentum transfer*, J.Phys.B: At.Mol.Opt.Phys. **32**, 3923–3937, 1999